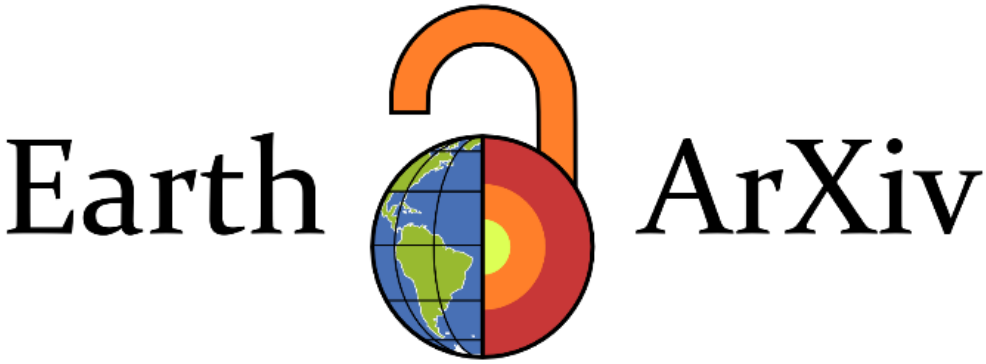

A novel experimental V-Sc olivine-melt oxybarometer for arc magmas

Enzo-Enrico Cacciatore[a], enzo-enrico.cacciatore@unige.ch, [0009-0007-4136-6219]

Ivano Gennaro[a], Ivano.Gennaro@unige.ch, [0000-0002-9903-781X]

Kalin Kouzmanov[a], Kalin.Kouzmanov@unige.ch, [0000-0002-7327-8949]

Alexandra Tsay[a], Alexandra.Tsay@unige.ch

Zoltán Zajacz[a], Zoltan.Zajacz@unige.ch, [0000-0001-6528-7717]

[a]Department of Earth Sciences, University of Geneva, Rue des Maraichers 13, 1205 Geneva, Switzerland

This manuscript is a **non-peer-reviewed preprint**. A **substantially revised and peer-reviewed version** has been published in: *Geochimica et Cosmochimica Acta*
https://doi.org/10.1016/j.gca.2025.12.025

A novel experimental V-Sc olivine-melt oxybarometer for arc magmas

Enzo-Enrico Cacciatore[a], Ivano Gennaro[a], Kalin Kouzmanov[a], Alexandra Tsay[a], and Zoltán Zajacz[a]

[a]Department of Earth Sciences, University of Geneva, Rue des Maraichers 13, 1205 Geneva, Switzerland

Corresponding author: Enzo-Enrico Cacciatore, enzo-enrico.cacciatore@unige.ch

Abstract

Redox conditions significantly affect phase equilibria, the availability and mobility of heterovalent elements, including volatiles (i.e., S) and metals (e.g., Fe, Cu) in silicate melts. Gaining a deeper understanding of the initial redox state of magmas may help better understand magmatic ore fertility, volcanic degassing, and the redox evolution of Earth's crust and atmosphere.

This study reports an optimized V and novel V-Sc olivine-melt oxybarometers, developed using existing V-partitioning data and new results from a series of fractional crystallization experiments. Experiments were conducted in a rapid-quench molybdenum-hafnium carbide pressure vessel apparatus equipped with a custom-designed hydrogen membrane for flexible, precise, and accurate oxygen fugacity (fO_2) control. They were performed at constant pressure (P = 200 MPa) and variable temperatures (T = 1019-870 °C), under water-saturated conditions at fO_2 ranging from -1 to +3.5 log units relative to the FMQ buffer. The impact of the system's composition (X) was evaluated by comparing two distinct liquid lines of descent (medium-K-calk-alkaline and shoshonitic) through simultaneous experiments using two capsules in parallel. The results show that the partition coefficient of V between olivine and melt ($D_V^{[Ol/melt]}$) is not systematically affected by varying P-T-X and highly correlates with changing fO_2, thus suggesting that the minor variations

observed on a global fO_2 scale rather reflect analytical and experimental uncertainties. The updated empirical calibrations allow the determination of logfO_2 as ΔFMQ from measured 1) $D_V^{[Ol/melt]}$ and 2) $K_{D[V/Sc]}^{[Ol/melt]}$, expressed by the following equations:

$$1)\ \Delta FMQ = -1.72333 \pm 0.0473 - \left(\frac{\log_{10}[(1.2273 - \log(D_V^{[Ol/melt]})) / (\log(D_V^{[Ol/melt]}) + 3.11912)]}{-0.09895 \pm 0.00175} \right)$$

for NBO/T (non-bridging oxygens per tetrahedrally coordinated cation) ≤ 0.6:

$$2)\ \Delta FMQ = (\log(K_{D[V/Sc]}^{[Ol/melt]}) + 0.98079 \pm 0.02244) / -0.20567 \pm 0.01231$$

In the logfO_2 range of FMQ -1 to FMQ +3.5, relevant for arc magmatism, and at hydrous conditions, both oxybarometers show 2σ calibration uncertainty below 0.5 log units. The updated and new V-based oxybarometers enhance robustness across a wide *P*-*T*-*X*-fO_2 range, enabling accurate quantification of the redox state of magmatic systems. They can, in turn, be applied to volcanic rocks ranging from basaltic to andesitic compositions by using suitable olivine-hosted silicate melt inclusions to reconstruct the redox history of deep-seated magma reservoirs in subduction zones. In addition, we demonstrate that the olivine–melt Fe_T-Mg exchange coefficient (where Fe_T is total iron expressed as FeO) correlates with changing fO_2 and can serve as an Fe-Mg oxybarometer within the calibrated range of this study. Owing to the rapid diffusion of Fe in olivine, this approach can record rapid redox fluctuations and provides complementary constraints to the more robust V-based oxybarometers.

Keywords: experimental oxybarometers, olivine-melt equilibrium, V-Sc partitioning, fractional crystallization, hydrous arc magmas

1. Introduction

The redox state of magmas affects the genesis of magmatic-hydrothermal ore deposits (Zajacz et al., 2011, 2012; Park et al., 2021; Farsang and Zajacz, 2025), volcanic degassing (Burgisser and Scaillet, 2007; Park et al., 2021; Métrich, 2022; Moretti and

Neuville, 2022; Ai et al., 2024; Farsang and Zajacz, 2025), and igneous phase equilibria in general. Oxygen fugacity (fO_2) is the principal thermodynamic variable used as a measure of the redox state of magmas. Its value is commonly expressed in reference to buffer assemblages such as fayalite-magnetite-quartz (FMQ) as $\log fO_2$ = FMQ ±x, where x equals a relative value below or above FMQ (Eugster, 1957; Ballhaus et al., 1991; Cicconi et al., 2020). In this study we use the definition for the FMQ buffer as outlined in Ballhaus et al. (1991). By controlling the oxidation state of heterovalent elements (i.e., Fe^{2+} vs. Fe^{3+}), fO_2 governs phase equilibria, polymerization of silicate melts and element partitioning between mineral, melts and fluids. Besides pressure (P) and temperature (T), it is a key driver of the geochemical differentiation of Earth's interior (Muan and Osborn, 1956; Carmichael, 1991; Frost, 1991; Kress and Carmichael, 1991; Brounce et al., 2015; Arató and Audétat, 2017; Moretti and Neuville, 2022). Regarding magma differentiation, fO_2 influences the direction of liquid lines of descent (LLD) and thus affects the physicochemical properties of a magmatic system (Frost, 1991; Mallmann and O'Neill, 2013; Arató and Audétat, 2017; Bucholz and Kelemen, 2019; Wang et al., 2019; Tassara et al., 2020; Cottrell et al., 2021; Marxer et al., 2021).

Magmatism at convergent plate margins is characterized by elevated fO_2 compared to their counterparts in other geodynamic settings (Aeolous Lee et al., 2005; Evans, 2012; Cottrell et al., 2021; Zhao et al., 2022). This characteristic may play an important role in the development of calc-alkaline differentiation trends and also leads to the fertility of magmatic hydrothermal Cu-Au-Mo ore systems (Lee et al., 2012; Chiaradia, 2014; Park et al., 2021; Ai et al., 2024). Despite its significance, the origin of magma oxidation in arc settings is still debated. It has been proposed to develop either due to the flux of oxidizing slab fluids into the mantle wedge (Evans, 2012; Kelley and Cottrell, 2012; Brounce et al., 2015; Cottrell et al., 2021) or during magma differentiation in response to the crystallization of Fe^{2+}-rich minerals or volatile loss (Sato, 1978; Aeolous Lee et al., 2005; Lee et al., 2010; Tang et al., 2018). Consequently, oxybarometers that can be applied to hydrous magmas over a broad P-T-compositional (X) range and that are resistant to low-temperature re-equilibration are essential for gaining a deeper understanding of the above processes (Osborn, 1959;

Ballhaus et al., 1991; Frost, 1991; Blundy et al., 2020; Cicconi et al., 2020; Moretti and Ottonello, 2022). One such method is based on Vanadium (V) partitioning between mafic minerals and silicate melt. Vanadium is a heterovalent element with multiple stable oxidation states (V^{2+}, V^{3+}, V^{4+}, and V^{5+}). It becomes increasingly incompatible in olivine with increasing fO_2, thus allowing the olivine/melt bulk partition coefficient of V ($D_V^{[Ol/melt]}$) to be used as an oxybarometer (Canil, 1997; Mallmann and O'Neill, 2013; Mallmann et al., 2022). According to Shishkina et al. (2018), V has low diffusivity making it more robust against post magmatic changes than other redox-sensitive elements (i.e., Fe). Numerous experimental studies have been published assessing the oxybarometric potential of V leading to the development of various empirical calibrations based on new input within the *P*-*T*-*X*-fO_2 parameter space (i.e., Canil, 1997; Shearer et al., 2006; Mallmann and O'Neill, 2013; Leuthold et al., 2023). However, only a few studies have calibrated the V-in-olivine oxybarometer at elevated pressure in the presence of hydrous melts, conditions typical of magma differentiation at convergent plate boundaries (Mallmann and O'Neill, 2009; Shishkina et al., 2018; Wang et al., 2019; Erdmann et al., 2024). The present study extends the existing dataset to lower temperature (T < 1030 °C) at high pressure (P = 200 MPa) and water-saturated conditions. Furthermore, the effect of melt composition was also tested by using medium-K-calk-alkaline (MKCA) and shoshonitic (SHOSH) starting compositions, bracketing the typical range of magma compositions at convergent plate margins. A prototype externally heated cold-seal pressure vessel apparatus equipped with a custom-designed hydrogen membrane was used to run the experiments, which facilitated both flexible, precise and accurate fO_2 control as well as rapid quenching (Alex and Zajacz, 2022; Farsang and Zajacz, 2025).The experiments follow a temperature-controlled fractional crystallization series with systematically varied fO_2, directly addressing the call of Marxer et al. (2021), who emphasized the key role of redox conditions in arc magma differentiation.

In turn, by combining the new data with preexisting experimental data using statistical analysis, we enhance the robustness and accuracy of V-in-olivine oxybarometry for hydrous

arc magmatic systems. Furthermore, we examine the Fe-Mg exchange coefficient between olivine and silicate melt as an additional tool for tracking redox conditions.

2. Experimental methods

2.1. Experimental strategy

To test the potential influence of silicate melt composition, two distinct hydrous basaltic compositions were used as initial starting material to represent typical MKCA and SHOSH magmatic series encountered in subduction zone settings based on literature data from the EarthChem database (Earthchem Portal, 2021). All experiments were conducted at P = 200 MPa and water-saturated conditions. The glass matrix of the run products constrained the starting material composition for the subsequent experiment within the same fractional crystallization series. This facilitated the tracing of individual LLDs while avoiding a high degree of crystallization. Fractional crystallization series experiments were conducted with both starting materials at 5 different fO_2 between FMQ-1 and FMQ+3.5 with a step size of about 1 log unit encompassing much of the range of Earth's magmatism. The temperature steps for each series were the following: 1030, 990, 960, 920, and 870 °C.

2.2. Starting material

As in fractional crystallization series experiments, a new starting composition is used at each temperature and fO_2 step, the use of a powdered synthetic starting material is preferred over the use of a starting glass (Nandedkar, 2014; Marxer et al., 2021). To prepare these, high-purity commercial oxide and silicate powders were utilized, except for sodium (Na) and potassium (K). The latter were added in the form of in-house-prepared K- and Na-rich aluminosilicate glasses (see Table S.1 in the supplementary material). A mixture of metallic Fe and Fe_2O_3 was used in proportion calculated for each experiment using the method of Kress and Carmichael (1991) to match the expected Fe^{2+}/Fe^{3+} ratio in the silicate melt at the target fO_2. In-house made trace element doped peralkaline aluminosilicate glass was used to introduce trace elements (5.4 wt.%, c.f. Table S.1). Their concentrations in the starting material was chosen similar to Nandedkar et al. (2014) to ensure that Henry`s law was not violated. All components were thoroughly homogenized in an agate mortar under

This manuscript is a **non-peer-reviewed preprint**. A **substantially revised and peer-reviewed version** has been published in: *Geochimica et Cosmochimica Acta*
https://doi.org/10.1016/j.gca.2025.12.025

ethanol. The solid starting materials were then dehydrated and stored in a vacuum desiccator. Compositions of the starting materials are summarized in Table 1.

Table 1. Major element composition (wt.%) of the starting materials.

No.	[a]Experiment	SiO_2	TiO_2	Al_2O_3	FeO-tot	MnO	MgO	CaO	P_2O_5	Na_2O	K_2O	Total-dry	[b]FeO/Fe_2O_3
1	E7.0_II_SB_A	50.6	0.9	16.0	8.9	0.2	9.6	10.2	0.2	2.6	0.7	100	0.43
2	E7.0_II_SB_B	51.1	1.1	14.4	8.4	0.2	9.0	9.0	0.7	2.7	3.4	100	0.44
3	E1.1_IV_H2_A	55.9	1.1	19.5	5.0	0.1	4.8	8.7	0.3	3.7	0.9	100	0.25
4	E1.1_IV_H2_B	55.4	1.1	19.2	4.7	0.2	4.1	7.2	1.1	3.8	3.3	100	0.23
5	E3.1_II_SB_A	55.9	1.1	18.8	5.5	0.2	4.9	8.8	0.4	3.5	0.9	100	0.28
6	E3.1_II_SB_B	55.4	1.0	18.8	4.9	0.2	4.1	7.4	1.0	3.9	3.3	100	0.27
7	E4.1_IV_H2_A	51.9	1.0	17.8	8.7	0.1	6.4	10.4	0.2	2.7	0.7	100	0.36
8	E4.1_III_H2_B	53.1	1.2	16.0	8.1	0.1	5.6	9.5	0.8	2.8	2.8	100	0.35
9	E4.1_IV_H2_B	53.1	1.2	16.0	8.1	0.1	5.6	9.5	0.8	2.8	2.8	100	0.35
10	E2.1_III_H2_A	51.8	1.0	18.5	8.0	0.2	5.8	10.5	0.3	3.1	0.8	100	0.39
11	E2.1_III_H2_B	52.9	1.3	16.9	7.8	0.2	4.8	8.6	0.9	3.4	3.3	100	0.38
12	E7.1_SB_II_A	53.3	1.2	19.3	6.7	0.2	4.8	10.0	0.3	3.2	0.9	100	0.44
13	E7.1_SB_II_B	53.5	1.3	18.2	6.6	0.3	4.1	8.3	0.9	3.4	3.4	100	0.44
14	E1.2_H2_A	59.8	1.3	19.1	3.8	0.2	3.6	6.6	0.5	4.1	1.1	100	0.26
15	E1.2_H2_B	57.3	1.1	20.5	3.4	0.2	3.6	6.6	0.9	3.9	2.5	100	0.28
16	E3.2_SB_A	57.4	1.2	18.9	5.3	0.2	4.2	7.8	0.4	3.8	0.8	100	0.29
17	E3.2_II_H2_A	57.4	1.2	18.9	5.3	0.2	4.2	7.8	0.4	3.8	0.8	100	0.29
18	E3.2_SB_B	56.2	1.0	19.4	4.9	0.2	3.8	6.9	1.1	3.9	2.6	100	0.29
19	E3.2_II_H2_B	56.2	1.0	19.4	4.9	0.2	3.8	6.9	1.1	3.9	2.6	100	0.29
20	E3.2_IV_H2_B	56.2	1.0	19.4	4.9	0.2	3.8	6.9	1.1	3.9	2.6	100	0.29
21	E5.2_H2_A	54.9	1.1	19.5	6.1	0.2	5.3	8.4	0.4	3.5	0.7	100	0.31
22	E4.2_II_H2_A	53.6	1.0	19.4	7.1	0.2	5.1	9.6	0.3	3.0	0.7	100	0.37
23	E4.2_H2_B	54.9	1.2	18.1	6.4	0.2	4.4	7.9	0.9	3.1	2.8	100	0.36
24	E4.2_II_H2_B	54.9	1.2	18.1	6.4	0.2	4.4	7.9	0.9	3.1	2.8	100	0.36
25	E2.2_III_H2_A	53.0	1.1	19.5	7.5	0.2	4.7	9.2	0.4	3.6	0.8	100	0.38
26	E2.2_III_H2_B	53.7	1.5	18.5	7.0	0.2	4.0	8.0	1.0	3.5	2.7	100	0.40

27	E7.2_II_SB_A	55.5	1.5	19.1	5.9	0.2	4.2	8.6	0.4	3.5	0.9	100	0.45
28	E7.2_II_SB_B	55.6	1.5	18.4	5.5	0.3	3.8	7.5	1.0	3.3	3.2	100	0.43
29	E4.3_H2_A	56.4	1.1	19.6	6.6	0.2	3.6	7.1	0.5	3.8	1.1	100	0.35

Table 1. (continued).

No.	[a]Experiment	SiO_2	TiO_2	Al_2O_3	FeO-tot	MnO	MgO	CaO	P_2O_5	Na_2O	K_2O	Total-dry	[b]FeO/Fe_2O_3
30	E2.3_II_H2_A	55.6	1.2	18.8	7.2	0.2	4.1	8.2	0.5	3.5	0.8	100	0.41
31	E2.3_II_H2_B	54.8	1.6	18.7	6.5	0.1	3.9	7.5	1.0	3.3	2.7	100	0.39
32	E7.3_SB_A	58.7	1.7	18.4	5.4	0.2	3.3	6.7	0.6	4.0	1.1	100	0.46

[a]Experiments ordered by decreasing temperature: .0, .1, .2, and .3 being equivalent to 1019, 990, 960, and 920 °C, respectively. fO_2 control is either through SB (solid buffer) or H2 (hydrogen membrane). A and B denote medium-K-calk-alkaline (MKCA) and shoshonitic (SHOSH) starting material, respectively. In the labeling system (e.g., E7.0_II_SB_A), the Roman numeral indicates the n-th experimental attempt.

[b]Calculated FeO/Fe_2O_3 ratio based on added Fe_2O_3- and metallic Fe-powder.

2.3. Capsule preparation

Pure Au capsules were used for experiments conducted at temperature below 1000 °C, while an $Au_{92.5}Pd_{7.5}$ (by wt.%) alloy was employed for temperature exceeding 1000 °C. Each experimental iteration consisted of two capsules (OD: 3 mm, ID: 2.8 mm, length:10 mm). These were loaded with dry synthetic starting powders (~20 mg) of either MKCA (labeled as “A” in Table 1) or SHOSH (“B”) composition and 2 mg of distilled water to ensure water saturation. The capsules were welded shut using a Lampert Puk V5 professional welder. They were tested afterwards for potential leaks by exposing them to 120 °C for 30 min and only capsules without weight loss were used for the experiments. To maintain the proximity between the two inner capsules, a larger holder capsule (5 mm OD, 4.7 mm ID, length: 12-20 mm) was employed, with one end sealed. Potential Fe loss was monitored using mass balance calculations, revealing only minor loss, with a maximum of less than 13 rel.%. observed in the most reducing experiments (FMQ -1, Table 3). A Co-CoO solid buffer (CCO) was employed for experiments conducted under reducing conditions at FMQ -1 due to technical limitations associated with the hydrogen buffer technique. For the

secondary quality assessment of redox control, a more oxidizing solid buffer (Re-ReO_2) was utilized to constrain fO_2 to FMQ +2.5. In both instances of applying solid buffers, a double capsule technique was implemented, where the solid buffer powder was contained within a partially open Pt capsule (4 mm OD, 3.7 mm ID, length: 11 mm) positioned behind the experimental capsules. Subsequently, all three inner capsules were enveloped within an outer Au capsule (5 mm OD, 4.4 mm ID, length: ~27.5 mm**)**, and adequate distilled water was added to preserve buffering capacities before sealing (for capsule design see supplementary Figure S.1). In the following sections, we distinguish experimental runs with fO_2 control achieved by solid buffer (SB) from those where a hydrogen membrane (H_2) was applied.

2.4. Experimental apparatus

Experiments were conducted in an externally heated cold-seal molybdenum-hafnium carbide (MHC) pressure vessel apparatus at the Mineral Resources and Geofluids Research Laboratory at the University of Geneva. Argon gas was used as a pressure medium monitored with an accuracy of < 20 bars by using a digital pressure transducer calibrated against a certified Ashcroft (Heise) analog gauge. An MHC vessel equipped with a single cold-seal extension was employed for SB runs. When using a CCO buffer, hydrogen (PH_2 = 10-13 bars at room temperature) was added to the argon pressure medium to extend the lifetime of the buffer (Alex and Zajacz, 2020). For H_2 runs, an MHC vessel was coupled with a semi-permeable hydrogen membrane (Shaw membrane), allowing flexible in-situ control of PH_2 while maintaining fast quench capabilities (Alex and Zajacz, 2022). The first set of experiments at 1030 °C was conducted under constant but higher than intended fO_2 conditions due to unrecognized reduced performance of the hydrogen membrane and therefore excluded for the fO_2 calibration of trace element-based olivine oxybarometry except for the CCO-runs (for run conditions of all experiments, see Table S.2).

Temperature control was ensured via K-type thermocouple with an accuracy of ±3 °C. The temperature inside the vessel was calibrated semi-annually against the external thermocouple by using internal thermocouples at P = 200 and 100 MPa (no significant

pressure effect observed). The temperature gradient within the hot zone was also estimated by using internal thermocouples of varying length. For both H_2- and SB-runs the temperature gradient along the capsules' length was below 10 °C. In the case of the applied double-capsule technique in SB-runs, the target temperature was adjusted to the capsule's center at 15 mm below the hot end, where the difference between the capsule's center and the cold end was about 10 °C. Once thermal stability was reached during SB runs, the capsules were dropped into the hot zone. The standard run procedure for H_2-runs was as follows: A bracketing approach was chosen to estimate the PH_2 within the vessel under run conditions and adjusted to the desired PH_2 if needed (Farsang and Zajacz, 2025). Note that on our apparatus, the Shaw membrane can be turned from supply to monitoring function by the closure of a single valve. All experiments began once steady-state equilibrium between external and internal PH_2 was established, at which point the capsule was dropped into the hot zone. The PH_2 was monitored using a factory-calibrated digital pressure-transducer with ±0.25% full-scale error (Alex and Zajacz, 2020). Depending on the target PH_2, three pressure transducers were used for the best precision and accuracy with the following ranges: I) 0–68.95 ±0.17 bar, II) 0–34.47 ±0.09 bar, and III) 0-2.068 ±0.005 bar. At a given fH_2, fO_2 inside the capsule was imposed by the water breakdown reaction ($2H_2+O_2 \leftrightarrow 2H_2O$) (Gorman and Nardella, 1962; Shaw, 1963; Hewitt, 1977; Gunter et al., 1979; Scaillet et al., 1992). The value of fH_2O at run conditions was calculated by using the equation of states of Churakov and Gottschalk (2003). The run fO_2 was recalculated considering the temperature gradient and fluctuations in applied pressure and PH_2 to obtain an uncertainty of the imposed fO_2. For some experimental SB-runs, temperature cycling with ±10 °C amplitude for around total 16 h was applied to enhance crystal growth similar to da Silva et al. (2017). Temperature oscillation was applied at the beginning of the experiment and completed in 6 cycles. High and low set temperatures were reached within 5 and 30 min, respectively, and then held constant for 1 h each to ensure thermal equilibrium. In experiment E5_2_A an amplitude of ±15 °C was applied. All experimental parameters are summarized in Table 2.

Table 2 Summary of run conditions.

Run	[a]SM	*t* (h)	[b]fH_2 (bar)	[c]±Δ fH_2 (bar)	logfO_2 (bar)	[d]±Δ logfO_2 (bar)	logfO_2 (ΔFMQ)	[d]±Δ logfO_2 (ΔFMQ)	*P* (bar)	[e]±Δ *P* (bar)	*T* (°C)	[f]±Δ *T* (bar)	T_{cyc} (°C)
E7_0_II-SB	A and B	18	nd	nd	-11.54	0.15	-0.87	0.15	2011	13	1019	10	nd
E1_1_IV-H2	A and B	60	0.46	0.17	-7.55	0.41	3.56	0.41	2004	67	990	10	nd
E3_1_II-SB	A and B	49	nd	nd	-8.57	0.14	2.54	0.15	1975	85	990	10	nd
E4_1_III-H2	B	59	7.06	0.07	-9.92	0.01	1.19	0.05	2016	13	990	10	nd
E4_1_IV-H2	A and B	60	7.41	0.32	-9.96	0.04	1.15	0.06	2020	38	990	10	nd
E2_1_III-H2	A and B	62	19.46	1.45	-10.80	0.07	0.31	0.08	2013	5	990	10	nd
E7_1_II-SB	A and B	48	nd	nd	-11.97	0.15	-0.86	0.16	1983	27	990	10	10
E1_2-H2	A and B	72	0.55	0.04	-8.22	0.06	3.37	0.08	2019	12	960	10	nd
E3_2-SB	A and B	56	nd	nd	-9.01	0.15	2.58	0.16	2044	12	960	10	10
E3_2_II-H2	A and B	28	1.88	0.08	-9.29	0.04	2.30	0.06	2007	55	960	10	nd
E3_2_IV-H2	B	106	1.86	0.02	-9.28	0.01	2.31	0.05	2018	15	960	10	nd
E5_2-H2	A	117	3.05	0.04	-9.32	0.38	2.27	0.39	2044	40	960	15	15
E4_2-H2	B	72	8.63	0.49	-10.61	0.05	0.97	0.07	2020	11	960	10	nd
E4_2_II-H2	A and B	72	8.20	0.40	-10.57	0.04	1.02	0.07	2020	5	960	10	nd
E2_2_III-H2	A and B	57	20.95	0.95	-11.37	0.02	0.22	0.06	2026	2	960	10	nd
E7_2_II-SB	A and B	48	nd	nd	-12.44	0.16	-0.85	0.17	2021	28	960	10	10
E4_3-H2	A	90	6.51	0.13	-11.11	0.02	1.15	0.06	2040	5	920	10	nd
E2_3_II-H2	A and B	87	19.00	0.22	-12.04	0.01	0.22	0.06	2025	3	920	10	nd
E7_3-SB	A	56	nd	nd	-13.10	0.17	-0.84	0.17	2007	29	920	10	10

"nd" = not determined.

[a]Starting material (see Table 1).

[b]fH_2 determined by bracketing PH_2; values are the average of the minimum and maximum pressures recorded during the run. See text for details.

[c]Uncertainty in fH_2 equals half the range of PH_2 (max-min).

[d]Propagated uncertainty based on uncertainty in fH_2, T and P using the water break down reaction with the equation of states of Churakov and Gottschalk (2003). For SB-runs, error propagation was based on the corresponding buffer equations (Frost 1991; Pownceby and O'Neill 1994). Conversion into ΔFMQ follows Ballhaus et al. (1991).

[e]Uncertainty in P is determined as for PH_2.

[f]Uncertainty in T from the temperature gradient along capsule lengths or from temperature cycling (T_{cyc}).

3. Analytical Methods

3.1. Sample preparation and backscattered electron (BSE)-imaging

After the experiments, all capsules were checked for conservation of mass. Consecutively, the capsules were pierced and checked for the presence of excess water visually and by heating them to 120 °C for 30 minutes and monitoring the weight loss during the process. The capsules were then vacuum-impregnated and embedded in epoxy resin and subsequently ground until sufficient run product material was exposed. This process was followed by polishing and carbon coating. The run products were first characterized by back scattered electron (BSE) imaging by using a Jeol JSM 7001F Scanning Electron Microscope. It served as a qualitative assessment of the textural distribution of different mineral phases and their identification. All pieces of analytical instrumentation utilized in this study are housed within the Department of Earth Sciences at the University of Geneva.

3.2. Electron probe microanalysis (EPMA)

Major and minor element concentrations (Si, Al, Ca, Mg, Fe, Na, K, Mn, Ti, P, Ni, and Cr) were determined by using a JEOL JXA-8200 Superprobe or later a Hyperprobe-JXA-IHP200F electron microprobe, utilizing wavelength dispersive spectrometers at an acceleration voltage of 15 kV. A beam current of 6 nA, accompanied by a spot size of 10 µm for the glass matrix, and 20 nA with a spot size of < 1 µm for mineral phases, were applied. Calibration of olivine and glass analyses were done by using various natural mineral and glass standards (glass Smithsonian A99 for Si and Al; olivine for Si and Mg; fayalite for Fe; albite for Na; wollastonite for Ca; orthoclase for K and Al; apatite for P_2O_5; nickel oxide for Ni; chromium oxide for Cr; and $MnTiO_3$ for Mn and Ti). Peak and background measurements

for all elements were set at 30 s and 15 s, respectively. To mitigate alkali loss, these were reduced to 20 and 10s for Na and K while measured first on respective detectors. In the case of olivine analysis, Al, Ti, and Ca were corrected for secondary fluorescence effects after the method of Gavrilenko et al. (2023) assuming an average grain radius of 10 µm. Secondary reference materials such as San Carlos olivine and the Smithsonian volcanic glasses VG2 and ML3BG were employed to ascertain the results' accuracy and precision. For further analytical details see supplementary material (Table S.3 - S.7 and Figure S.2 and 3). In addition, element maps were acquired by wavelength-dispersive X-ray electron probe microanalysis (WDX-EPMA) at 15 kV, 20 nA, using a focused beam and dwell time of 350 ms and processed using XMapTools 4.3 (Lanari et al., 2014, 2019).

3.3. Laser ablation inductively coupled plasma mass spectrometry (LA-ICP-MS)

3.3.1. Data acquisition

The LA-ICP-MS analysis was performed using an ESL-193 HE laser ablation system from coupled to an Agilent 8900 triple quadrupole ICP-MS. The nebulizer gas (Ar) and a carrier gas (He) flow rates for were 0.85 ± 0.02 l/min and 0.85 l/min, respectively. The instrument was tuned to ThO/Th ≤ 0.3 %, mass-21/mass-42 ~0.2 % and 238U/232Th of ~1.0 using the glass reference material NIST610. The USGS basaltic glass standard GSD-1g was used as an external standard, whereas NIST610 was measured in each analysis block for quality control. In addition, glass reference material NIST617 was analyzed to correct for the contribution of the polyatomic interference $^{29}Si^{16}O$ to the ^{45}Sc signal. Run product glasses were ablated at an energy density of ~3 J/cm^2, a repetition rate of 7 Hz and a laser spot size of 30 µm. Each acquisition consisted of 35 s of background collection followed by 40 s of signal counting time. Mineral phases were ablated at an energy density of ~2 J/cm^2 and a repetition rate of 4 Hz. The laser spot size was from 7 to 10 µm and the signal duration varied from 2 to 30 s. On-peak dwell times were set to 10 ms for most isotopes. For olivines the dwell times were increased for certain elements (see Table S.5). Each analysis block consisted of ~35 analyses of unknowns bracketed by two measurements of GSD-1g and one measurement of each NIST610 and NIST617. Due to small crystal sizes in the run products,

the signals can be short (e.g., ~2 s) or represent a mixture of the mineral phase and the glass matrix. Because Cs, Nb, Th and U are highly incompatible in olivine, they were used as proxies to identify and exclude signal contamination from glass matrix ablation (Nandedkar, 2014).

3.3.2. LA-ICP-MS data processing

The raw data of olivine and glass were first cleaned for signal spikes by an in-house Python algorithm. Data from olivine and glass analyses were processed using the SILLS program (Guillong et al., 2008) and the Iolite software (Paton et al., 2011), respectively. Limits of detection (LOD) calculations followed the method of Longerich et al. (1996). Based on the NIST617 analysis, the contribution of the polyatomic interference $^{29}Si^{16}O$ to ^{45}Sc signal was corrected (typically about 1 µg/g artificial signal on Sc) similar to the method of Jenner and O'Neill (2012). Olivine quantification used 100 wt.% major element oxide total as internal standard, while glass quantification used Silicon (^{29}Si) from EPMA measurements (SiO_2) as the internal standard. For glass analysis, LA-ICP-MS signal intervals (~20 s) excluded significant Cr spikes and plateaus, which resulted from small spinel crystals within the ablated glass volume. For olivine, only signal intervals free of proxy elements for glass contamination were chosen as schematically summarized in Fig. 1. Analyses showing clear downhole elemental fractionation were omitted. Concentrations are reported as geometric means ± standard errors (1σ) from valid measurement spots. However, these values may still reflect sampling biases in olivine signal intervals, as the small spot size increases susceptibility to downhole elemental fractionation over acquisition time. A more accurate approach is to apply a signal stitching technique on the raw spectra to form a composite sample signal of multiple individual sampling intervals similar to the approach of Rauchenstein-Martinek et al. (2014). To carry out the raw signal stitching, an in-house developed Python algorithm was applied (schematically illustrated in Figure S.4). The stitched signal for each sample was processed using the SILLS program, selecting only segments free from downhole elemental fractionation and employing the same standard blocks as in the conventional approach. This procedure also allows the exclusion of false

positive sample intervals (i.e., spinel inclusions) from the signal integration. The resulting uncertainties on concentration values are solely analytical. This approach improves counting statistics, lowers detection limits, and in most cases yields smaller uncertainties compared to the sample variance derived from conventional data processing. The resulting contents of representative elements for both conventional and stitched signal integration are within 10 rel.% (Figure S.5). Due to the increased precision and accuracy, the data obtained by the signal stitching procedure are used for interpretation. For detailed information about precision and accuracy assessment of olivine and silicate glass see Table S.5, Figure S. 6 - S.9.

3.4. Raman spectroscopy

Confocal Raman microspectrometry was applied to quantify the water content in the run product glasses. Raman spectra were collected using a confocal LabRAM HR Evolution (HORIBA Scientific) Raman spectrometer with an 800 mm focal length. The spectral resolution was ~0.5 cm^{-1}. A grating of 600 lines/mm and a confocal hole of 100 µm were employed. A 100 mW Toptica TopMode 405 laser source (Toptica Photonics) with a wavelength of 405 nm was used for excitation. The spectra were acquired in backscattering geometry using an Olympus LMPlanFLN 50X long working distance objective. For each spectrum, three accumulations of 30 s each were taken in the spectral window of 50 – 4000 cm^{-1}. To prevent laser heating-induced damage to the glass, the laser energy on the sample surface was reduced to about 2 mW by using a density filter. The Raman spectrum was quantified using SilicH2O (van Gerve and Namur, 2023). Reference materials included two andesitic glasses (#159 and #155), containing 5.74 and 5.54 wt.% water, respectively, measured by FTIR (Zajacz et al., 2005, 2012), and an in-house water-free glass.

3.5. QEMSCAN and ImageJ

To obtain a quantitative assessment of mineral proportions, an automated mineral analysis and textural imaging were performed using a FEI QEMSCAN® Quanta 650F facility. The system is equipped with two Bruker QUANTAX light-element energy dispersive X-ray

spectrometer (EDS) detectors. Analyses were conducted at high vacuum, accelerating voltage of 25 kV, and a beam current of 10 nA on carbon-coated polished epoxy mounts. Analyses were performed in Field-Image mode (Pirrie et al., 2004). In total, between 9 and 15 individual fields were measured per sample, with 1000 µm per field, and point spacing of 1 µm. The standard 1000 counts per point were acquired, yielding a limit of detection of approximately 2 wt.% per element for mineral classifications. Measurements were performed using iMeasure v5.3.2 software, and data processing using the iDiscover® v5.3.2 software package. The final results consist of: 1) high-quality spatially resolved and fully quantified mineralogical maps; 2) BSE images with identical resolution as the mineralogical maps; 3) X-ray element distribution maps. The results of QEMSCAN analysis were compared with those obtained using ImageJ (Schindelin et al., 2012) applied to the BSE image overviews acquired via SEM imaging (section 3.1). Due to similarities in contrast and brightness, the ImageJ algorithm cannot reliably distinguish between different ferromagnesian minerals, between the glass matrix and plagioclase, or between spinel and apatite. Therefore, the ImageJ-based analysis serves primarily as a secondary assessment of mineral proportions, particularly given that the QEMSCAN analysis was performed on a reduced area compared to the full sample surface and carries higher uncertainties for very small mineral grains (e.g., spinel and apatite) due to single-pixel resolution limits.

3.6. Statistical analysis and error propagation

In this study, the distribution of geochemical data as a function of experimental parameters (P, T, X, and fO_2) was evaluated using linear and non-linear regression in OriginPro (OriginLab, 2024), employing iterative least squares via the Levenberg–Marquardt algorithm (Marquardt, 1963; Moré, 1978). Model fit significance was assessed by p-values for each parameter estimate (e.g., slope, intercept, inflection point, or asymptote), testing the null hypothesis that the parameter equals zero (i.e., that the model fit is not significantly different from a simpler baseline). A p-value below 0.05 (rejection of null hypothesis) indicates statistical significance with a default display cutoff of 0.0001. The fitting procedure was considered converged at a X^2-tolerance of $1*10^{-9}$. OriginPro automatically generates

1000 interpolated points to plot smooth fitted curves. Fit quality is expressed by the coefficient of determination (R^2) and the root mean squared error (RMSE) values. In addition, principal component analysis (PCA) and a correlation matrix (CorMat) were applied to log-normalized geochemical dataset to explore parameter relationships and identify underlying correlations.

The bulk partition coefficient of heterovalent elements as a function of fO_2 is known to follow a sigmoidal trend (Mallmann et al., 2022), where the central portion of the curve can be approximated by a linear regression. However, sigmoidal fitting is sensitive to uncertainties in the top and bottom asymptotes. While these asymptotes are mathematically essential for defining the full sigmoidal function, they correspond to fO_2 where the calibrated oxybarometer is not typically applied. To reduce the impact of these uncertainties on the key parameters of interest (i.e., the curve center and slope), a two-step sigmoidal fitting approach was used: 1) An initial exploratory sigmoidal fit was performed. Due to the limited availability of experimental data at extreme fO_2 conditions (outside FMQ -5 to +5, c.f. Erdmann et al. (2024)), this step often yielded high uncertainties in the asymptote estimates, which dominated the total fitting uncertainty (c.f. Motulsky and Christopoulos, 2004). 2) In the second fitting step, the top and bottom asymptotes were fixed to the values obtained in the primary fit, using their 95% confidence intervals. This constraint allowed for a more robust estimation of the central parameters, and the remaining uncertainties were subsequently incorporated into the error propagation for each oxybarometer calibration.

For error propagation (standard error, SE) we provide the equations for linear and sigmoidal functions as follows:

1) For linear function:

$$1\text{SE Uncertainty}(\Delta FMQ) = \sqrt{\left(\Delta y/m\right)^2 + \left(\left[-(y-t)/m^2\right] * \Delta m\right)^2 + \left(-\Delta t/m\right)^2} \quad (1)$$

409 The variables denote the respective parameters in the linear equation $y = m*x+t$, where *y*
410 represents the partition or exchange coefficient, *t* is the intercept, *m* is the slope, and Δ
411 corresponds to the 1σ uncertainty of each parameter.

412 2) For sigmoidal function:

413 $$1SE\ Uncertainty\ (\Delta FMQ) = \sqrt{(\Delta LOGx0)^2 + \left(\frac{\sqrt{\left[\frac{\sqrt{\Delta A2^2+\Delta A1^2}}{y-A1}\right]^2+\left[\frac{(A2-A1)*\Delta y}{(y-A1)^2}\right]^2+\left[\frac{(A2-A1)*\Delta A2}{(y-A1)^2}\right]^2}}{\left[\left(\frac{A2-A1}{y-A1}\right)-1\right]*\ln(10)*p}\right)^2 + \left(\left[\frac{\log_{10}\left[\left(\frac{A2-A1}{y-A1}\right)-1\right]}{p^2}\right]*\Delta p\right)^2} \quad (2)$$

414 The variables denote the respective parameters in the sigmoidal function
415 $y = A1+\left((A2-A1)\Big/\left[1+10^{(LOGx0-x)*p}\right]\right)$, where *y* represents the partition or exchange coefficient,
416 *LOGx0* the center, *p* the hill slope and *x* the logfO_2 (ΔFMQ). *A1* and *A2* are the bottom and
417 top asymptote, respectively. Δ-notation indicates the 1σ uncertainty of each parameter.

418 After defining individual oxybarometers through regression fitting, their performance
419 was evaluated using two criteria: 1) The propagated uncertainty: The total uncertainty
420 (combining both fitting and analytical components) was assessed as the median propagated
421 uncertainty across the calibration dataset. This approach reduced the influence of outliers
422 with exceptionally high analytical uncertainty. 2) The reproducibility of the calibration
423 dataset: The predictive success of each oxybarometer can be estimated by the percentage
424 of calibration data points it can reproduce within a defined fO_2-threshold of 0.5 ΔFMQ. This
425 threshold reflects the typical combined uncertainties associated with experimental fO_2
426 measurements and model predictions in high-temperature magmatic systems (Erdmann et
427 al., 2024). A prediction was considered successful if the difference between the calculated
428 fO_2 (including its 2σ propagated uncertainty) and the measured fO_2 (including 2σ uncertainty
429 on fO_2 control of 0.2 ΔFMQ, if not defined otherwise) was less than the 0.5 ΔFMQ threshold
430 value.

The performance of both published and newly developed oxybarometers was evaluated by comparing calculated and measured fO_2 values. Hereby, two parameters were used to quantify their performance: 1) Pearson's R^2 for an assessment of precision (Prec.) and 2) the proximity to the line of equality (equiline) valuing the accuracy (Acc.) of reproducing the measured fO_2. Precision and accuracy assessment were combined by using the so-called concordance correlation coefficient (CCC, Lawrence, 1989) together with the RMSE. The CCC ranges from 0 to 1, with values closer to 1 indicating better model performance. In addition, the 2σ propagated uncertainty (Unc.) for each oxybarometer was evaluated as well.

4. Results

4.1. Quality control measures

This section overviews essential prerequisites of successful experiments, addresses limitations, and assesses the quality of fO_2 control during experiments. Experiments are considered successful if the following requirements are fulfilled: 1) the mass of experimental capsules is conserved; 2) the presence of excess water is confirmed; 3) stable redox conditions are attained throughout the experimental run; 4) a chemically closed system is maintained (i.e., negligible Fe-loss); and 5) the run product glass and olivines are chemically homogeneous.

The masses of the inner and double capsules were measured before and after the experimental runs, revealing no significant differences for most of the experiments (Table 3). As all experimental capsules were filled with abundant distilled water (around 10 wt.%), fluid bubbles observed as cavities, are considered as an effect of excess water trapped in the viscous melt-crystal mush upon quenching (Marxer et al., 2021). Raman spectrometry applied on the run product glasses (Table 3) results in water concentrations consistently around 5.5 wt.% and corresponds well to the expected values at water saturation at the experimental run conditions (T = 1019-920 °C and P = 200 MPa (Lesne et al., 2011; Botcharnikov et al., 2015)). This confirms that water in the excess fluid phase was not

458 significantly diluted by other volatile species such as N_2 and CO_2 and therefore the activity
459 of water can be considered equal to 1.

460 Water-saturated conditions facilitate precise control of fO_2 via the imposed hydrogen
461 during experiments, with key parameters being fluctuations in PH_2, pressure (i.e., PAr), and
462 temperature. Except for PH_2, the same applies to SB-runs. The combination of these key
463 parameters allows obtaining a propagated uncertainty on the imposed fO_2 as listed in Table
464 2. For all experiments, logfO_2 uncertainty was < 0.20 log units (ΔFMQ), except for two runs
465 (E1.1_IV_H2 and E5.2_H2), which showed higher uncertainties of ~0.4 log-units. For
466 E1.1_IV_H2, notable PH_2 fluctuations were observed, while E5.2_H2 was subject to
467 temperature-cycling (±15 °C).

468 Maintaining a chemically closed system is essential for successful experiments.
469 Potential Fe-loss to the Au-capsule and the occurrence of cryptocrystalline to amorphous
470 aggregates of residual powder linked to hercynitic spinel formation are key concerns. Iron
471 loss was estimated through optimized mass balance regression, combining BSE-derived
472 estimates for mineral proportions with their EPMA-based compositions. Table 3 shows that
473 values for the Fe-loss (ΔFe_{loss} in rel.%) are in general below 5 % relative to the bulk FeO
474 content of the starting material except for most reducing runs (CCO-buffer, ≤ 13 rel.% Fe-
475 loss). The sum of the squared residuals from the mass balance calculation (ΣR^2) shows
476 mostly values below 1, except for one experiment (Table 3). For further details regarding
477 the mass balance calculation see Table S.8. Overall, we conclude that due to the applied
478 low temperature (T ≤ 1020 °C) and the use of pure Au-capsules for all runs (except
479 E7.0_II_SB), Fe-loss does not significantly impact the fractional crystallization series in this
480 study.

481 In two-thirds of the experiments, we observed minor patches of unreacted powder
482 associated with hercynitic spinel which appears to be sealed off from the actual experimental
483 load by overgrown plagioclase. This experimental artifact is referred to as residual powder
484 artifact (RPA). It is considered negligible, as no systematic correlation is observed between
485 their presence and any intensive parameter (i.e., fO_2) or chemical variable (e.g., the V-Sc-,

Fe-Mg exchange and V partition coefficient between olivine and melt), nor do they influence the LLD. Statistical analysis, including a CorMat and conditional density plots with RPA as a categorical factor, revealed no significant relationships. While conditional density plots suggest slightly more frequent RPA occurrence at lower temperatures, the correlation matrix showed no meaningful correlation (see Figure S.10 and Table S.9). For example, in experiment E4_2_H2_II_B, optimized mass balance calculations yielded a good fit ($\Sigma R^2 = 0.90$). The estimated mineral proportions (in rel.%) are glass (Gl): 94.00, olivine (Ol): 3.08, Pl: 2.44, spinel (Spl): 0.16 and apatite (Ap): 0.32. These values align with those obtained from QEMSCAN (Gl: 94.88, Ol: 2.34, Pl: 2.73, RPA: < 0.10, Spl+Ap < 0.10) and ImageJ combined (Gl+Pl: 96.24, Ol+RPA: 3.20, Spl+Ap: 0.57). For detailed information see supplementary material (Table S.10 and Figure S.11). The mineral proportions derived from optimized mass balance, QEMSCAN and imageJ collectively support the statistical evidence that RPA presence does not affect the LLD. In addition, all experiments showed residual liquid being quenched to a homogeneous glass (c.f. Table 4 and subsequent section).

4.2. Attainment of equilibrium

The attainment of equilibrium was mainly assessed by time series experiments at constant fO_2 (FMQ +2.5), T = 960 °C and P = 200 MPa and variable run duration (28, 56, and 106 h) including a comparison of SB- (i.e., $ReReO_2$) with H_2-runs. As shown in Fig. 2 the Fe-Mg and V-Sc exchange coefficients are consistent within 2σ standard error independent of run duration. Only the MKCA sample at the shortest run duration falls outside the 2σ range. All experiments were carried out at a significantly longer run duration than 28 h, except for E7.0_II_SB (18 h, 1019 °C, FMQ -0.87) to prevent the exhaustion of the CCO buffer. The run duration was increased with decreasing temperature (Table 2). The homogeneity of run product glasses and olivines serves as secondary indication of reaching chemical equilibrium. Element distribution maps for the redox-sensitive element Fe demonstrate chemical homogeneity, confirming the attainment of redox equilibrium (Fig. 3). Due to its fast diffusion under magmatic conditions it is sensitive to detect any redox disequilibrium (Shea et al., 2023).

This manuscript is a **non-peer-reviewed preprint**. A **substantially revised and peer-reviewed version** has been published in: *Geochimica et Cosmochimica Acta*
https://doi.org/10.1016/j.gca.2025.12.025

4.3. Experimental run products

4.3.1. Textural and phase assemblage overview

Olivine crystallizes alongside various other minerals (according to their frequency of occurrence: spinel, plagioclase, clinopyroxene (Cpx), apatite, orthopyroxene (Opx), amphibole (Amp), ilmenite (Ilm) and phlogopite (Phl)). Regarding glass and olivine, all major- (i.e., FeO), minor- and most trace elements (i.e., V) show low variations (Tables 4 and 5). In general, olivine occurs as subhedral crystals with rounded margins containing occasionally spinel and/or plagioclase inclusions. The olivine stability field at 920 °C seems to be restricted to fO_2 between FMQ -0.86 and FMQ +1.25, and preferably for MKCA starting material. Only for this starting material, the E7.X_SB-fO2- series (approx. FMQ -0.87) showed olivine at four distinct temperatures (1019, 990, 960, and 920 °C). Therefore, we use these experiments to highlight the textual relationship between olivine and co-crystallizing mineral phases as a function of temperature, as summarized in Fig. 4. Especially in experiment E7.3_SB_A (920 °C) the olivine appears only in very small amounts and reduced crystal size.

Table 3 Summary of run products: water content, residual powder artifact (RPA), and relative Fe-loss.

Sample	[a]Δ Fe-loss-%	[a]ΣR²	[b]RPA	[c]Δ-mass$_{cap}$ (mg)	[c]Δ-mass$_{dried}$ (mg)	[d]H_2O (wt.%)	[d]±Δ H_2O (wt.%)
E7.0_II_SB_A	10.43	0.41	x	0.04	2.28	5.51	0.16
E7.0_II_SB_B	10.62	0.37	o	0.04	2.34	5.53	0.16
E1.1_IV_H2_A	8.18	0.24	x	0.18	1.4	6.37	0.31
E1.1_IV_H2_B	3.37	0.11	o	0.02	1.43	5.31	0.24
E3.1_II_SB_A	1.18	0.00	x	nd	0.81	5.50	0.15
E3.1_II_SB_B	0.14	0.69	o	-1.1	1.84	5.46	0.17
E4.1_IV_H2_A	4.14	0.00	o	0	1.48	5.31	0.17
E4.1_III_H2_B	0.27	0.00	o	-0.01	1.49	5.75	0.17
E4.1_IV_H2_B	6.18	0.02	o	-0.01	1.53	5.76	0.17
E2.1_III_H2_A	3.23	0.21	x	-0.05	1.33	6.05	0.15
E2.1_III_H2_B	1.40	[e]3.76	o	-0.08	1.41	6.51	0.19
E7.1_SB_II_A	12.15	0.01	o	nd	nd	6.93	0.16
E7.1_SB_II_B	12.77	0.64	o	nd	1.5	6.95	0.17
E1.2_H2_A	1.19	0.30	x	0	1.17	5.50	0.76

This manuscript is a **non-peer-reviewed preprint**. A **substantially revised and peer-reviewed version** has been published in: *Geochimica et Cosmochimica Acta*
https://doi.org/10.1016/j.gca.2025.12.025

E1.2_H2_B	3.70	0.09	x	-0.02	1.22	6.69	0.37
E3.2_SB_A	3.00	0.08	x	nd	0.48	5.79	0.16
E3.2_II_H2_A	4.08	0.75	x	0.01	1.21	5.49	0.23
E3.2_SB_B	0.24	0.00	o	nd	1.98	5.62	0.20
E3.2_II_H2_B	0.91	0.01	x	-0.01	1.3	6.20	0.16
E3.2_IV_H2_B	0.15	0.16	x	0.02	1.29	6.81	0.20
E5.2_H2_A	0.69	0.24	o	nd	1.31	5.71	0.17
E4.2_II_H2_A	3.29	0.28	o	-0.03	1.44	6.60	0.30

Table 3. (continued).

Sample	[a]ΔFe-loss-%	[a]ΣR²	[b]RPA	[c]Δ-mass$_{cap}$ (mg)	[c]Δ-mass$_{dried}$ (mg)	[d]H_2O (wt.%)	[d]±Δ H_2O (wt.%)
E4.2_H2_B	5.55	0.39	o	-0.06	1.34	6.46	0.17
E4.2_II_H2_B	2.46	0.90	x	-0.1	1.26	6.32	0.16
E2.2_III_H2_A	3.18	0.04	o	0.08	1.28	6.71	0.19
E2.2_III_H2_B	2.10	0.46	o	0.01	1.45	7.44	0.18
E7.2_II_SB_A	10.75	0.02	x	-0.06	0.32	7.15	0.17
E7.2_II_SB_B	10.61	0.19	x	0.01	1.13	6.46	0.17
E2.3_II_H2_A	11.30	0.21	o	-0.03	1.32	7.36	0.34
E2.3_II_H2_B	4.93	0.02	x	-0.02	1.36	8.00	0.37
E7.3_SB_A	11.18	0.56	x	0.25	2.74	7.42	0.22

"nd" = not determined.

[a]Relative Fe-loss (%) from mass balance regression; ΣR^2 gives the sum of squared residuals. Details in supplement tables, Table S.8 - S.10).

[b]Rresidual starting powder (RPA) detected (x) or not detected (o).

[c]Δ-m_{Cap} and Δ-m_{-dried} are changes in capsule mass during the experiment and after piercing/drying, respectively. "nd" indicates the capsule was not recovered intact. Capsule integrity confirmed by residual water.

[d]H_2O contents by Raman spectroscopy with propagated 1σ standard deviation (SD). Elevated values in some glasses may reflect systematic overestimation due to baseline correction artifacts.

[e]Outlier of mass balance calculation, which is traced back to a misfit for Ca and Si, potentially due to undetected clinopyroxene.

4.3.2. The chemical composition of run product glass and olivine

Comparing the geometric mean ($\mu_{[geo.]}$) with its sample variation (standard deviation, 1σ SD) serves as an indicator for the homogeneity of both glass (Table 4) and

549 olivine (Table 5). Hereby, the median value of the coefficient of variation (CV [%]
550 = 1SD)/$\mu_{[geo.]}$ x100) is used (Stanley and Lawie, 2007). Glass composition demonstrates
551 generally low values for all major (< 3 %) and minor (< 13 %) elements. For most of the trace
552 elements, the CV is below 10 %, with a few exceptions for Cr and Ni (Table S.6. and S.11).
553 In the run product glasses, FeO varies from 3.00±0.02 to 7.05±0.03 wt.%, and MgO from
554 1.60±0.01 to 4.51±0.02 wt.%, both decreasing with decreasing temperature. Vanadium
555 ranges from 80.0±1.0 to 320.0±4.0 µg/g, and Sc from 24.7±0.8 to 59.5±1.2 µg/g.

556 In olivine, the CV values for all major-, minor- and most trace elements are mostly
557 below 2, 10 and 20 % respectively. Only samples E7.3_SB_A and E3.2_II_B show higher
558 values for some trace elements (Na, P, Cr, Ti, Yb and Ga, Table S.4, S.7. and S.12). Besides
559 the perspective of point analysis, element distribution maps were acquired on olivines for
560 representative samples as outlined in subsection 4.3.1. The most sensitive elemental redox
561 proxies (i.e., Fe) demonstrate no significant chemical zonation (Fig. 3). FeO content in
562 olivine range from 8.60±0.01 to 26.11±0.11 wt.%, while V-content varies from 1.9±0.1 to
563 35.1±2.2 µg/g. For both elements, their content increases with decreasing fO_2, and to a
564 lesser extent with decreasing temperature. The corresponding values of MgO range from
565 34.19±0.10 to 49.56±0.11 wt.%. Scandium varies between 11.8±0.5 and 70.1±4.8 µg/g and
566 shows a very weak positive correlation with decreasing temperature which is associated with
567 an increase in polymerization of the silicate melt (i.e., non-bridging oxygens per tetrahedrally
568 coordinated cation, NBO/T).

569

This manuscript is a **non-peer-reviewed preprint**. A **substantially revised and peer-reviewed version** has been published in: *Geochimica et Cosmochimica Acta*
https://doi.org/10.1016/j.gca.2025.12.025

570 Table 4 Composition of the glass run product (including Sc, V, Cs and U).

Sample	[a]SiO_2 (wt.%)	[a]TiO_2 (wt.%)	[a]Al_2O_3 (wt.%)	[a]FeO (wt.%)	[a]MnO (wt.%)	[a]MgO (wt.%)	[a]CaO (wt.%)	[a]N_2O (wt.%)	[a]K_2O (wt.%)	[a]P_2O_5 (wt.%)	[a]Total (wt.%)	[a]n	[b]Sc µg/g	[b]V µg/g	[b]Cs µg/g	[b]U µg/g	[b]n	[c]NBO/T
E7.0_II_SB_A	50.00	1.17	18.13	6.30	0.18	4.51	9.42	2.97	0.79	0.31	93.78	29	45.9	250	102	27.2	14	0.608
	(0.07)	(0.01)	(0.06)	(0.09)	(0.01)	(0.02)	(0.02)	(0.03)	(0.01)	(0.02)	(0.2)		(0.91)	(3.1)	(0.51)	(0.18)		0.554
E7.0_II_SB_B	50.29	1.22	17.17	6.14	0.24	3.86	7.78	3.20	3.21	0.89	94.00	35	45.2	263	115	30.8	15	0.344
	(0.05)	(0.01)	(0.04)	(0.05)	(0.01)	(0.02)	(0.02)	(0.02)	(0.02)	(0.02)	(0.07)		(0.5)	(2.08)	(0.48)	(0.32)		0.335
E1.1_IV_H2_A	56.35	1.24	17.99	3.50	0.16	3.36	6.23	3.88	0.99	0.44	94.15	35	59.5	320	114	29	12	0.451
	(0.03)	(0.01)	(0.02)	(0.02)	(0.01)	(0.01)	(0.02)	(0.02)	(0.01)	(0.01)	(0.04)		(1.16)	(3.72)	(0.91)	(0.32)		0.418
E1.1_IV_H2_B	54.20	1.03	19.44	3.11	0.18	3.32	6.23	3.62	2.33	0.86	94.31	35	50	270	93.2	25.2	13	0.508
	(0.04)	(0.02)	(0.02)	(0.02)	(0.01)	(0.01)	(0.02)	(0.02)	(0.01)	(0.02)	(0.05)		(1.05)	(2.51)	(0.45)	(0.17)		0.496
E3.1_II_SB_A	53.59	1.07	17.67	4.94	0.19	3.88	7.27	3.50	0.76	0.39	93.27	44	51	265	95.2	24.7	17	0.472
	(0.05)	(0.01)	(0.05)	(0.04)	(0.01)	(0.02)	(0.01)	(0.02)	(0.01)	(0.01)	(0.08)		(0.63)	(1.66)	(0.5)	(0.18)		0.606
E3.1_II_SB_B	52.91	0.99	18.30	4.58	0.14	3.59	6.50	3.68	2.41	0.98	94.05	45	50.1	260	88.7	24.4	14	0.560
	(0.03)	(0.01)	(0.03)	(0.04)	(0.01)	(0.02)	(0.01)	(0.02)	(0.01)	(0.02)	(0.08)		(0.67)	(0.82)	(0.56)	(0.12)		0.503
E4.1_IV_H2_A	52.18	0.99	18.09	6.73	0.14	3.74	7.76	3.14	0.80	0.33	93.90	30	42.1	251	108	30.1	14	0.464
	(0.04)	(0.02)	(0.05)	(0.03)	(0.01)	(0.02)	(0.04)	(0.01)	(0.01)	(0.01)	(0.06)		(1.11)	(1.94)	(1.01)	(0.27)		0.608
E4.1_III_H2_B	51.34	1.11	17.79	6.33	0.13	3.59	7.17	2.90	2.66	0.86	93.86	44	37.1	239	101	26.5	13	0.554
	(0.03)	(0.01)	(0.02)	(0.02)	(0.01)	(0.01)	(0.03)	(0.01)	(0.01)	(0.01)	(0.05)		(0.48)	(9.1)	(2.29)	(0.6)		0.344
E4.1_IV_H2_B	51.87	1.12	18.05	6.03	0.12	3.46	7.09	2.93	2.66	0.86	94.17	30	31.1	222	92.2	23	14	0.335
	(0.03)	(0.02)	(0.02)	(0.03)	(0.01)	(0.02)	(0.01)	(0.02)	(0.01)	(0.01)	(0.05)		(0.28)	(1.7)	(0.73)	(0.15)		0.451
E2.1_III_H2_A	50.13	1.06	18.25	7.05	0.18	4.49	8.94	2.96	0.65	0.37	94.10	30	49.4	260	95	23.7	14	0.418
	(0.03)	(0.02)	(0.02)	(0.03)	(0.01)	(0.01)	(0.02)	(0.01)	(0.01)	(0.01)	(0.05)		(0.38)	(1.93)	(0.52)	(0.2)		0.508
E2.1_III_H2_B	49.87	1.31	17.80	7.05	0.15	3.98	7.45	3.23	2.45	0.95	94.22	30	51.4	258	89.1	23.1	13	0.496
	(0.03)	(0.02)	(0.02)	(0.03)	(0.01)	(0.01)	(0.02)	(0.02)	(0.01)	(0.02)	(0.04)		(0.5)	(1.4)	(0.25)	(0.18)		0.472
E7.1_SB_II_A	51.87	1.39	17.90	5.49	0.21	3.96	8.04	3.26	0.85	0.41	93.40	35	47.4	243	104	26.5	8	0.606
	(0.05)	(0.01)	(0.04)	(0.03)	(0.01)	(0.03)	(0.02)	(0.02)	(0.01)	(0.01)	(0.1)		(0.57)	(1.36)	(0.3)	(0.24)		0.560
E7.1_SB_II_B	52.07	1.40	17.21	5.08	0.26	3.52	7.04	3.11	2.97	0.90	93.58	35	49.3	278	92.6	23.7	8	0.503
	(0.04)	(0.01)	(0.05)	(0.03)	(0.01)	(0.02)	(0.01)	(0.02)	(0.02)	(0.02)	(0.07)		(0.41)	(3.05)	(0.4)	(0.07)		0.464

571

This manuscript is a **non-peer-reviewed preprint**. A **substantially revised and peer-reviewed version** has been published in: *Geochimica et Cosmochimica Acta*
https://doi.org/10.1016/j.gca.2025.12.025

572 Table 4 (continued).

Sample	[a]SiO_2 (wt.%)	[a]TiO_2 (wt.%)	[a]Al_2O_3 (wt.%)	[a]FeO (wt.%)	[a]MnO (wt.%)	[a]MgO (wt.%)	[a]CaO (wt.%)	[a]N_2O (wt.%)	[a]K_2O (wt.%)	[a]P_2O_5 (wt.%)	[a]Total (wt.%)	[a]n	[b]Sc µg/g	[b]V µg/g	[b]Cs µg/g	[b]U µg/g	[b]n	[c]NBO/T
E1.2_H2_A	57.84	0.96	18.28	3.17	0.13	2.92	5.13	4.05	1.18	0.49	94.14	34	46.5	250	96.8	26.8	11	0.276
	(0.04)	(0.02)	(0.03)	(0.02)	(0.01)	(0.01)	(0.02)	(0.03)	(0.01)	(0.02)	(0.05)		(0.73)	(4.02)	(0.67)	(0.38)		0.285
E1.2_H2_B	56.19	1.13	18.54	3.00	0.22	3.01	5.18	3.49	2.50	0.81	94.09	34	53.4	246	102	25.9	12	0.378
	(0.04)	(0.02)	(0.02)	(0.02)	(0.01)	(0.01)	(0.02)	(0.02)	(0.01)	(0.02)	(0.04)		(1.25)	(2.94)	(0.66)	(0.45)		0.374
E3.2_SB_A	55.53	1.19	17.11	4.61	0.17	3.28	6.34	3.54	0.66	0.48	92.88	36	47.8	237	95.6	23.7	10	0.356
	(0.13)	(0.01)	(0.06)	(0.02)	(0.01)	(0.01)	(0.01)	(0.02)	(0.01)	(0.02)	(0.1)		(0.41)	(3.23)	(0.47)	(0.13)		0.360
E3.2_II_H2_A	55.38	1.10	18.25	4.58	0.16	3.53	6.17	3.70	0.72	0.49	94.10	30	52.7	254	96.1	24.4	18	0.339
	(0.06)	(0.01)	(0.04)	(0.03)	(0.01)	(0.02)	(0.02)	(0.02)	(0.01)	(0.02)	(0.05)		(0.88)	(7.41)	(0.81)	(0.25)		0.446
E3.2_SB_B	53.70	0.99	18.31	4.35	0.16	3.16	5.75	3.53	2.06	1.00	93.00	37	49.6	233	89.6	22.8	12	0.440
	(0.15)	(0.01)	(0.03)	(0.01)	(0.01)	(0.01)	(0.01)	(0.02)	(0.01)	(0.02)	(0.16)		(0.6)	(2.21)	(0.49)	(0.17)		0.428
E3.2_II_H2_B	53.86	0.95	18.91	4.22	0.15	3.41	5.81	3.53	2.30	0.93	94.08	50	51.3	239	86.6	24.6	11	0.439
	(0.04)	(0.01)	(0.03)	(0.02)	(0.01)	(0.01)	(0.01)	(0.02)	(0.01)	(0.01)	(0.04)		(1.13)	(2.52)	(0.44)	(0.36)		0.521
E3.2_IV_H2_B	54.12	0.95	19.13	4.01	0.16	3.23	5.65	3.62	2.37	0.98	94.22	41	53.4	266	102	25	14	0.490
	(0.03)	(0.01)	(0.03)	(0.02)	(0.01)	(0.01)	(0.01)	(0.02)	(0.01)	(0.02)	(0.06)		(0.81)	(2.51)	(0.91)	(0.3)		0.276
E5.2_H2_A	53.45	1.08	18.29	5.38	0.20	4.11	6.75	3.40	0.61	0.41	93.71	35	53.5	295	99.8	25.4	6	0.285
	(0.06)	(0.02)	(0.08)	(0.03)	(0.01)	(0.02)	(0.1)	(0.04)	(0.01)	(0.01)	(0.05)		(1.28)	(10.14)	(2.08)	(0.48)		0.378
E4.2_II_H2_A	52.94	1.06	18.37	6.20	0.20	3.41	6.66	3.53	1.03	0.42	93.82	40	57.9	267	116	28	11	0.374
	(0.06)	(0.01)	(0.03)	(0.03)	(0.01)	(0.01)	(0.03)	(0.02)	(0.01)	(0.02)	(0.08)		(0.86)	(2.08)	(0.85)	(0.59)		0.356
E4.2_H2_B	52.78	1.14	18.22	5.42	0.15	3.32	6.77	2.94	2.53	0.92	94.20	25	45.9	264	82.9	22.2	9	0.360
	(0.05)	(0.02)	(0.03)	(0.03)	(0.01)	(0.02)	(0.02)	(0.02)	(0.01)	(0.02)	(0.04)		(0.86)	(1.98)	(1.21)	(0.28)		0.339
E4.2_II_H2_B	52.15	1.13	18.57	5.65	0.15	3.36	6.80	2.95	2.71	0.83	94.32	35	47	279	83.1	22.3	14	0.446
	(0.04)	(0.01)	(0.02)	(0.02)	(0.01)	(0.01)	(0.02)	(0.02)	(0.01)	(0.02)	(0.05)		(0.48)	(2.51)	(0.34)	(0.18)		0.440
E2.2_III_H2_A	51.68	1.16	17.49	6.68	0.12	3.82	7.68	3.23	0.71	0.43	93.02	27	50.3	254	95.8	24.6	11	0.428
	(0.04)	(0.01)	(0.03)	(0.03)	(0.01)	(0.02)	(0.03)	(0.03)	(0.01)	(0.02)	(0.07)		(0.39)	(1.52)	(0.51)	(0.14)		0.439
E2.2_III_H2_B	51.19	1.43	17.46	6.07	0.12	3.59	7.00	3.09	2.47	0.96	93.38	29	48.9	246	88.9	23.5	10	0.521
	(0.03)	(0.01)	(0.02)	(0.03)	(0.01)	(0.01)	(0.02)	(0.01)	(0.02)	(0.02)	(0.05)		(0.75)	(2.19)	(0.25)	(0.23)		0.490

573

This manuscript is a **non-peer-reviewed preprint**. A **substantially revised and peer-reviewed version** has been published in: *Geochimica et Cosmochimica Acta*
https://doi.org/10.1016/j.gca.2025.12.025

Table 4 (continued).

Sample	[a]SiO_2 (wt.%)	[a]TiO_2 (wt.%)	[a]Al_2O_3 (wt.%)	[a]FeO (wt.%)	[a]MnO (wt.%)	[a]MgO (wt.%)	[a]CaO (wt.%)	[a]N_2O (wt.%)	[a]K_2O (wt.%)	[a]P_2O_5 (wt.%)	[a]Total (wt.%)	[a]n	[b]Sc µg/g	[b]V µg/g	[b]Cs µg/g	[b]U µg/g	[b]n	[c]NBO/T
E7.2_II_SB_A	55.13	1.58	17.35	4.97	0.17	3.09	6.37	3.70	0.99	0.55	93.89	44	48.9	238	122	30.3	9	0.385
	(0.04)	(0.01)	(0.03)	(0.02)	(0.01)	(0.02)	(0.03)	(0.02)	(0.01)	(0.01)	(0.06)		(1.05)	(5.85)	(0.51)	(0.46)		0.349
E7.2_II_SB_B	54.53	1.29	18.35	4.38	0.20	2.78	5.99	3.49	2.86	0.77	94.63	45	47.1	173	100	26.8	8	0.276
	(0.05)	(0.01)	(0.03)	(0.03)	(0.01)	(0.01)	(0.02)	(0.02)	(0.01)	(0.02)	(0.05)		(1.14)	(2.39)	(0.47)	(0.51)		0.333
E4.3_H2_A	57.99	0.94	17.71	4.56	0.16	2.35	4.83	3.76	1.13	0.52	93.95	45	45.9	152	97.9	29.8	14	0.283
	(0.03)	(0.01)	(0.02)	(0.02)	(0.01)	(0.01)	(0.02)	(0.03)	(0.01)	(0.01)	(0.05)		(0.52)	(1.22)	(1.31)	(0.19)		0.212
E2.3_II_H2_A	56.75	1.07	17.18	5.53	0.15	2.41	5.57	3.54	0.91	0.55	93.66	39	39.9	186	115	33.6	13	0.385
	(0.04)	(0.01)	(0.02)	(0.03)	(0.01)	(0.01)	(0.01)	(0.03)	(0.01)	(0.02)	(0.05)		(1.47)	(1.65)	(0.61)	(0.94)		0.349
E2.3_II_H2_B	56.24	0.99	18.21	4.94	0.13	2.12	4.67	3.46	2.72	0.65	94.12	45	25.1	143	120	34	13	0.276
	(0.04)	(0.01)	(0.02)	(0.02)	(0.01)	(0.01)	(0.02)	(0.02)	(0.01)	(0.01)	(0.04)		(1.43)	(1.15)	(0.3)	(0.63)		0.333
E7.3_SB_A	60.97	0.86	16.15	3.50	0.11	1.60	4.28	3.94	1.34	0.37	93.11	32	24.7	80.3	128	28.9	11	0.283
	(0.07)	(0.01)	(0.03)	(0.04)	(0.01)	(0.01)	(0.01)	(0.03)	(0.01)	(0.01)	(0.04)		(0.76)	(1.05)	(1.19)	(0.31)		0.212

"n" = the number of analyses for each analytical technique. Uncertainties are 1σ standard errors (SE) in parentheses. Values below detection limit (BDL) are reported as "< µg/g". Elemental concentrations are rounded according to magnitude and analytical precision.

[a]EPMA analysis.

[b]LA-ICP-MS analysis.

[c]Non-bridging oxygen per tetrahedrally coordinated cation (NBO/T); calculated using Eq. (3) given by Zajacz and Tsay (2019), which is based on Mysen and Richet (2005).

This manuscript is a **non-peer-reviewed preprint**. A **substantially revised and peer-reviewed version** has been published in: *Geochimica et Cosmochimica Acta*
https://doi.org/10.1016/j.gca.2025.12.025

584

585 Table 5 Composition (including Sc, V, Cs and U) of the olivine run phase.

Sample	[a]SiO_2 wt.%	[a]FeO wt.%	[a]MnO wt.%	[a]MgO wt.%	[a]CaO wt.%	[a]Na_2O wt.%	[a]Total wt.%	[a]n	[b]Sc µg/g	[b]V µg/g	[b]Ni µg/g	[b]Cs µg/g	[b]U µg/g	[b]n
E7.0_II_SB_A	38.76	18.32	0.34	43.07	0.20	BDL	100.9	29	15.42	17.47	376.5	BDL	0	21
	(0.06)	(0.12)	(0.01)	(0.08)	(0.01)	< 103	(0.07)		(0.41)	(0.29)	(7.79)	< 0.113	(0)	
E7.0_II_SB_B	38.99	19.7	0.6	41.5	0.27	BDL	101.31	13	16.29	16.07	460	BDL	0	16
	(0.1)	(0.22)	(0.01)	(0.16)	(0.04)	< 104	(0.09)		(0.9)	(0.58)	(18.01)	< 0.256	(0)	
E1.1_IV_H2_A	40.94	10.23	0.37	48.34	0.11	0.01	100.31	30	14.13	1.88	1438	BDL	0	25
	(0.04)	(0.08)	(0.01)	(0.08)	(0.01)	(0.01)	(0.06)		(0.37)	(0.09)	(10.37)	< 0.118	(0)	
E1.1_IV_H2_B	41.13	8.6	0.48	49.56	0.07	0.02	100.11	28	30.75	2.38	1350	BDL	0	14
	(0.06)	(0.1)	(0.01)	(0.11)	(0.01)	(0.01)	(0.07)		(0.58)	(0.11)	(12.72)	< 0.158	(0)	
E3.1_II_SB_A	40.15	14.33	0.48	45.73	0.12	BDL	101.08	40	13.96	3.21	1274	BDL	0	22
	(0.03)	(0.05)	(0.01)	(0.05)	(0.01)	< 105	(0.05)		(0.67)	(0.18)	(16.46)	< 0.281	(0)	
E3.1_II_SB_B	40.4	13.65	0.28	46.25	0.13	BDL	100.99	35	20.58	3.86	1376	BDL	0	20
	(0.02)	(0.03)	(0.01)	(0.04)	(0.01)	< 105	(0.04)		(0.97)	(0.26)	(23.12)	< 0.329	(0)	
E4.1_IV_H2_A	39.32	18.39	0.28	41.36	0.17	0.02	99.75	19	11.8	4.1	714.3	BDL	0	20
	(0.02)	(0.04)	(0.01)	(0.05)	(0.01)	(0.01)	(0.06)		(0.46)	(0.16)	(10.88)	< 0.174	(0)	
E4.1_III_H2_B	39.09	17.91	0.27	41.72	0.19	0.02	99.43	31	12.57	3.01	759.3	BDL	0	15
	(0.03)	(0.03)	(0.01)	(0.03)	(0.01)	(0.01)	(0.04)		(1.2)	(0.3)	(22.59)	< 0.279	(0)	
E4.1_IV_H2_B	39.36	18.07	0.28	41.67	0.19	0.02	99.79	21	12.8	3.97	852.4	BDL	0	15
	(0.03)	(0.03)	(0.01)	(0.03)	(0.01)	(0.01)	(0.04)		(0.6)	(0.19)	(13.66)	< 0.227	(0)	
E2.1_III_H2_A	39.08	19.08	0.38	40.59	0.19	0.01	99.51	32	15.53	10.92	475.7	BDL	0	21
	(0.06)	(0.05)	(0.01)	(0.04)	(0.01)	(0.01)	(0.08)		(0.65)	(0.22)	(10.37)	< 0.197	(0)	
E2.1_III_H2_B	38.93	19.94	0.35	39.91	0.21	0.02	99.56	37	18.66	11.35	230.3	BDL	0	13
	(0.03)	(0.06)	(0.01)	(0.04)	(0.01)	(0.01)	(0.06)		(0.85)	(0.36)	(12.25)	< 0.252	(0)	
E7.1_SB_II_A	39.46	17.38	0.45	42.52	0.16	BDL	100.15	22	18.42	13.25	186.9	BDL	0	28
	(0.04)	(0.04)	(0.01)	(0.13)	(0.01)	< 104	(0.17)		(0.98)	(0.39)	(8.05)	< 0.33	(0)	
E7.1_SB_II_B	39.44	17.7	0.71	42.28	0.19	BDL	100.5	29	19.9	15.56	458.8	BDL	0	7

This manuscript is a **non-peer-reviewed preprint**. A **substantially revised and peer-reviewed version** has been published in: *Geochimica et Cosmochimica Acta*
https://doi.org/10.1016/j.gca.2025.12.025

	(0.04)	(0.09)	(0.01)	(0.08)	(0.01)	< 105	(0.15)		(1.79)	(0.71)	(20.55)	< 0.647	(0)	

Table 5 (continued).

Sample	[a]SiO_2 wt.%	[a]FeO wt.%	[a]MnO wt.%	[a]MgO wt.%	[a]CaO wt.%	[a]Na_2O wt.%	[a]Total wt.%	[a]n	[b]Sc µg/g	[b]V µg/g	[b]Ni µg/g	[b]Cs µg/g	[b]U µg/g	[b]n
E1.2_H2_A	40.9	10.93	0.25	47.73	0.08	0.02	100.3	30	23.44	2.84	2322	BDL	0	18
	(0.03)	(0.05)	(0.01)	(0.05)	(0.01)	(0.01)	(0.05)		(0.59)	(0.13)	(15.99)	< 0.126	(0)	
E1.2_H2_B	40.86	10.12	0.53	48.13	0.08	0.01	100.1	28	29	2.67	2528	BDL	0	16
	(0.03)	(0.09)	(0.01)	(0.06)	(0.01)	(0.01)	(0.04)		(0.7)	(0.14)	(18.61)	< 0.148	(0)	
E3.2_SB_A	40.02	14.28	0.4	45.34	0.09	BDL	100.47	30	25.23	4.22	1242	BDL	0	17
	(0.03)	(0.09)	(0.01)	(0.11)	(0.01)	< 109	(0.06)		(1.27)	(0.28)	(22.87)	< 0.375	(0)	
E3.2_II_H2_A	40.03	14.55	0.4	44.24	0.13	0.02	99.69	26	21.36	4.13	1862	BDL	0	14
	(0.03)	(0.05)	(0.01)	(0.05)	(0.01)	(0.01)	(0.05)		(1.06)	(0.28)	(32.34)	< 0.315	(0)	
E3.2_SB_B	40.05	14.08	0.42	45.44	0.10	BDL	100.42	29	29.39	4	1518	BDL	0	16
	(0.04)	(0.06)	(0.01)	(0.08)	(0.01)	< 110	(0.1)		(1.65)	(0.33)	(31.32)	< 0.487	(0)	
E3.2_II_H2_B	40.25	13.42	0.34	45.14	0.12	0.02	99.66	26	22.97	4.31	1654	BDL	0	20
	(0.03)	(0.03)	(0.01)	(0.04)	(0.01)	(0.01)	(0.05)		(1.99)	(0.5)	(44.68)	< 0.46	(0)	
E3.2_IV_H2_B	40.23	13.36	0.33	45.41	0.09	0.02	99.72	28	23.36	3.64	1500	BDL	0	20
	(0.03)	(0.03)	(0.01)	(0.04)	(0.01)	(0.01)	(0.06)		(0.7)	(0.17)	(16.49)	< 0.152	(0)	
E5.2_H2_A	40.32	14.5	0.45	45.51	0.10	BDL	101.11	33	18.93	3.25	963.4	BDL	0	25
	(0.05)	(0.03)	(0.01)	(0.04)	(0.01)	< 104	(0.05)		(0.58)	(0.11)	(9.03)	< 0.19	(0)	
E4.2_II_H2_A	39.14	20.13	0.41	39.81	0.12	0.02	99.8	25	19.72	5.95	642.8	BDL	0	18
	(0.04)	(0.1)	(0.01)	(0.09)	(0.01)	(0.01)	(0.04)		(0.79)	(0.24)	(12.46)	< 0.16	(0)	
E4.2_H2_B	39.11	18.66	0.41	40.92	0.14	0.02	99.46	29	24.04	6.65	777	BDL	0	20
	(0.03)	(0.05)	(0.01)	(0.04)	(0.01)	(0.01)	(0.07)		(0.84)	(0.25)	(14.85)	< 0.169	(0)	
E4.2_II_H2_B	39.42	18.54	0.33	41.11	0.13	0.02	99.77	26	24.13	6.07	763.8	BDL	0	17
	(0.02)	(0.03)	(0.01)	(0.03)	(0.01)	(0.01)	(0.04)		(0.74)	(0.21)	(11.94)	< 0.139	(0)	
E2.2_III_H2_A	38.92	20.8	0.28	40.2	0.15	0.02	100.56	47	16.16	9.58	359.2	BDL	0	23
	(0.02)	(0.05)	(0.01)	(0.02)	(0.01)	(0.01)	(0.05)		(0.49)	(0.22)	(7.84)	< 0.147	(0)	

This manuscript is a **non-peer-reviewed preprint**. A **substantially revised and peer-reviewed version** has been published in: *Geochimica et Cosmochimica Acta*
https://doi.org/10.1016/j.gca.2025.12.025

E2.2_III_H2_B	38.82	19.5	0.31	40.57	0.15	0.02	99.57	38	23.59	10.52	498.5	BDL	0	15
	(0.03)	(0.04)	(0.01)	(0.04)	(0.01)	(0.01)	(0.05)		(1.09)	(0.35)	(15.49)	< 0.301	(0)	
E7.2_II_SB_A	39.04	19.89	0.45	40.61	0.14	BDL	100.31	19	28.33	22.42	496.3	BDL	0	20
	(0.05)	(0.15)	(0.01)	(0.09)	(0.01)	< 110	(0.17)		(1.48)	(0.72)	(18.67)	< 0.38	(0)	

588 Table 5 (continued).

Sample	[a]SiO_2	[a]FeO	[a]MnO	[a]MgO	[a]CaO	[a]Na_2O	[a]Total	[a]n	[b]Sc	[b]V	[b]Ni	[b]Cs	[b]U	[b]n
	wt.%	wt.%	wt.%	wt.%	wt.%	wt.%	wt.%		µg/g	µg/g	µg/g	µg/g	µg/g	
E7.2_II_SB_B	39.11	19.58	0.64	40.86	0.16	BDL	100.52	12	26.65	17.84	187.2	BDL	0	7
	(0.05)	(0.14)	(0.01)	(0.13)	(0.01)	< 109	(0.08)		(1.98)	(0.75)	(13.49)	< 0.569	(0)	
E4.3_H2_A	38.56	21.58	0.6	38.4	0.10	0.02	99.47	44	25.9	6.05	523.3	BDL	0	6
	(0.02)	(0.05)	(0.01)	(0.03)	(0.01)	(0.01)	(0.06)		(1.86)	(0.59)	(29.09)	< 0.563	(0)	
E2.3_II_H2_A	37.75	26.06	0.51	34.43	0.14	0.02	99.1	32	19.9	11.53	277.7	BDL	0	11
	(0.02)	(0.06)	(0.01)	(0.04)	(0.01)	(0.01)	(0.05)		(1.37)	(0.58)	(16.99)	< 0.269	(0)	
E2.3_II_H2_B	37.79	25.92	0.46	34.43	0.14	0.02	98.98	24	24.28	10.56	463.2	BDL	0	15
	(0.04)	(0.06)	(0.01)	(0.05)	(0.01)	(0.01)	(0.06)		(1.18)	(0.43)	(16.32)	< 0.251	(0)	
E7.3_SB_A	37.24	26.91	0.56	34.19	0.12	0.02	99.25	21	70.1	35.11	180	BDL	0	2
	(0.05)	(0.11)	(0.01)	(0.1)	(0.01)	(0.01)	(0.08)		(4.8)	(2.24)	(39.29)	< 0.848	(0)	

589 See Table 4 for definitions of “n,” uncertainty reporting, detection limits, and rounding conventions.

590 [a]EPMA analysis.

591 [c]LA-ICP-MS analysis. Cs and U included to illustrate their incompatibility in olivine and suitability as proxy elements for distinguishing
592 olivine from the glass matrix.

593

This manuscript is a **non-peer-reviewed preprint**. A **substantially revised and peer-reviewed version** has been published in: *Geochimica et Cosmochimica Acta*
https://doi.org/10.1016/j.gca.2025.12.025

4.4. Partitioning of redox-sensitive elements between olivine and melt

This section explores partitioning behavior of hetero-valent elements between olivine and silicate melt and their potential to be used as redox sensors in the relevant arc magmatic fO_2 range. Element contents were normalized to those of monovalent elements with the same charge and similar ionic radius to derive exchange coefficients that are less sensitive to temperature and compositional variations in melt and olivine.

4.4.1. Exploration of potential redox-sensitive element partitioning

To explore the dataset, we applied a combined PCA and CorMat approach using the following inputs: 1) major element compositions of olivine, glass, and starting material; 2) intensive parameters (*P*, *T,* and fO_2); 3) modeled (MELTS, H_2O_{mod}), and measured H_2O contents; and 4) silicate melt properties such as ASI (aluminum saturation index, in mol) and NBO/T. NBO/T was calculated following Eq. (3) from Zajacz and Tsay (2019), which is based on the formulation of Mysen and Richet (2005).

A second CorMat was generated using a reduced dataset that included partition coefficients ($D_{[i]}^{[Ol/melt]}$) for compatible elements (*i*) in olivine with special focus on redox-sensitive indicators: $D_{[V]}^{[Ol/melt]}$, $D_{[Fe]}^{[Ol/melt]}$, Fe-Mg exchange coefficient ($K_{D[Fe_T/Mg]}^{[Ol/melt]}$, defined as the molar Fe_T/Mg-ratio, where Fe_T is derived from total FeO-content of both olivine and silicate glass), and V-Sc exchange coefficient ($K_{D[V/Sc]}^{[Ol/melt]}$). For further details see Table S.13, S14 and Figure S.12 in the supplementary material. $D_{[V]}^{[Ol/melt]}$ and $K_{D[V/Sc]}^{[Ol/melt]}$ showed the strongest negative correlation with changing fO_2, followed by $D_{[Fe]}^{[Ol/melt]}$ and $K_{D[Fe_T/Mg]}^{[Ol/melt]}$ with moderate to strong correlation, which are consistent with their known redox sensitivity (Osborn, 1959; Carmichael and Ghiorso, 1990; Ehlers et al., 1992; Mysen, 2006; Blundy et al., 2020; Burnham et al., 2020; Leuthold et al., 2023). $D_{[i]}^{[Ol/melt]}$ values for other heterovalent elements demonstrated weak or non-significant correlations within the studied fO_2 range. Based on these findings, the three relevant redox-sensitive systems (V, V-Sc, and Fe-Mg) are discussed in order of decreasing significance in the following subsections.

620 *4.4.2. V-based oxybarometry between olivine and melt*

621 Among all elements analyzed, V demonstrates the strongest correlation with fO_2. Fig.
622 5 compares $D^{[Ol/melt]}_{[V]}$ with $K_{D[V/Sc]}^{[Ol/melt]}$ as well as the partitioning of Sc ($D^{[Ol/melt]}_{[Sc]}$) and V-content in
623 the glass and olivine as a function of fO_2. Although the $\log(D^{[Ol/melt]}_{[Sc]})$ ranges from -0.624 to
624 0.453, it demonstrates no apparent dependence on fO_2 and it appears instead to be
625 influenced by NBO/T and temperature (Fig. 5c). The V distribution in both glass and olivine
626 (subsection 4.3.2) shows a more pronounced systematic variation with fO_2 (Fig. 5d). While
627 the $\log(D^{[Ol/melt]}_{[V]})$ varies from -0.359 to -2.232, $\log(K_{D[V/Sc]}^{[Ol/melt]})$ shows values from -0.681 to -
628 1.844, both with increasing fO_2 (Fig. 5a and b). The $K_{D[V/Sc]}^{[Ol/melt]}$ is less affected by increasing
629 NBO/T with decreasing temperature, hence increasing fractional crystallization. Linear
630 regression fits for the two starting materials (MKCA vs. SHOSH) show no significant
631 difference, as their 95 % confidence intervals largely overlap across the studied fO_2 range.
632 The strong negative correlations for both $D^{[Ol/melt]}_{[V]}$ and $K_{D[V/Sc]}^{[Ol/melt]}$ with logfO_2 (ΔFMQ) can be
633 expressed by the following linear regressions including ±1SE, whereas the outlier
634 E7.3_SB_A was excluded from the fitting process for equation Eq. (3):

635 $$\Delta FMQ = (\log(D_V^{[Ol/melt]})_{(y)} + 1.30027^{*}_{(t)} \pm 0.02464^{*}_{(\Delta t)}) / -0.2214_{(m)} \pm 0.01307_{(\Delta m)} \quad (3)$$

636 $$\Delta FMQ = (\log(K_{D[V/Sc]}^{[Ol/melt]})_{(y)} + 0.98079_{(t)} \pm 0.02244_{(\Delta t)}) / -0.20567_{(m)} \pm 0.01231_{(\Delta m)} \quad (4)$$

637 In the special case for Eq. (3) the intercept* was fixed for the fitting process. Both its value
638 and corresponding fitting error are derived from an exploratory fitting process by using
639 $D^{[Ol/melt]}_{[V]}$ instead of $\log(D^{[Ol/melt]}_{[V]})$ (see Figure S.13). Equations (3) and (4) calculate logfO_2
640 (ΔFMQ) generally within a 2σ propagated median uncertainty (cf. Eq. (1)) of 0.38 and
641 0.44 log units, respectively. Note that the propagated analytical uncertainty of both the
642 partition and exchange coefficient is included. Regarding the calibration dataset (n = 32)
643 they show within 0.5 ΔFMQ threshold value a success rate of reproducibility of 84.4% and
644 90.6%, respectively.

This manuscript is a **non-peer-reviewed preprint**. A **substantially revised and peer-reviewed version** has been published in: *Geochimica et Cosmochimica Acta*
https://doi.org/10.1016/j.gca.2025.12.025

4.4.3. Fe-Mg exchange coefficient between olivine and melt

The $\log(K_{D[Fe_T/Mg]}^{[Ol/melt]})$ demonstrates potential as an oxybarometer at redox conditions above ~FMQ -0.5 as it follows a well-defined sigmoidal trend with changing fO_2 (Fig. 6). While melt composition (MKCA vs. SOSH) displays no significant effect on it, as the 95 % confidence intervals overlap (Fig. 6a), the $\log(K_{D[Fe_T/Mg]}^{[Ol/melt]})$ seems to be influenced by temperature and melt polymerization (NBO/T), alongside fO_2 (Fig. 6a and b). This effect appears to be stronger with decreasing fO_2, as reflected by a sharp increase in the fayalite component of olivine (expressed as molar fraction of fayalite, X_{Fay}, Fig. 6c), which also captures the influence of temperature (Fig. 6a). To better understand the behavior of the $\log(K_{D[Fe_T/Mg]}^{[Ol/melt]})$, we model it as a function of fO_2, incorporating the variability from NBO/T and X_{Fay}:

$$\begin{aligned}\log(K_{D[Fe_T/Mg]}^{[Ol/melt]})_{\mathrm{mod}} &= -0.4523 - 0.0253*\Delta FMQ - 0.0116*\Delta FMQ^2 \\ &+0.0009*\Delta FMQ^3 - 0.1593*(1+3*C)*3*NBO/T \\ &\text{with } C\text{:} \\ &for\ X_{Fay}(mol) > 0.225:\ C = X_{Fay}(mol) - 0.225 \\ &for\ X_{Fay}(mol) \le 0.225:\ C = 0\end{aligned} \quad (5)$$

The modelled Fe-Mg exchange coefficient ($\log(K_{D[Fe_T/Mg]}^{[Ol/melt]})_{\mathrm{mod}}$) as a function of fO_2 is illustrated by Fig. 6b. A polynomial regression model comparing $\log(K_{D[Fe_T/Mg]}^{[Ol/melt]})$ and $\log(K_{D[Fe_T/Mg]}^{[Ol/melt]})_{\mathrm{mod}}$ yields a correction equation, providing a compositionally adjusted Fe-Mg exchange coefficient ($\log(K_{D[Fe_T/Mg]}^{[Ol/melt]})_{cor}$) that accounts for the NBO/T and X_{Fay} effects:

$$\begin{aligned}\log(K_{D[Fe_T/Mg]}^{[Ol/melt]})_{cor} &= 1.0868*\log(K_{D[Fe_T/Mg]}^{[Ol/melt]})_{measured} + 0.0517*NBO/T \\ &-1.1534*X_{Fay} - 2.287*\log(K_{D[Fe_T/Mg]}^{[Ol/melt]})_{measured}*X_{Fay}\end{aligned} \quad (6)$$

A sigmoidal regression fit of the $\log(K_{D[Fe_T/Mg]}^{[Ol/melt]})_{cor}$ versus fO_2 relationship defines an oxybarometer. The resulting equation (including ±1SE uncertainty on the fitting parameters)

is defined with fixed lower and upper asymptotes at -2.2 (estimated by experimental data at very oxidizing conditions, see Figure S. 14) and -0.48 (derived from the canonical value of 0.3+0.03 uncertainty after Roeder and Emslie, 1970), respectively, as follows:

$$\Delta FMQ = LOGx0 - \left(\log_{10}\left[{1.51851}/{(y+2.2)} \right] - 1 \right) \Big/ p \quad (7)$$

with LOGx0 = 8.08156±0.28604, p = -0.18550±0.00927 and y = $\log(K_{D[Fe_T/Mg]}^{[Ol/melt]})_{cor}$. For more details about the generation of equations Eq. (5) and (6), see supplementary material S4 and Table S.15. Equation (7) calculates logfO_2 (ΔFMQ) generally within a 2σ propagated median uncertainty of 0.92 log units. Applying Eq. (7) on the calibrated dataset shows a success rate of reproducibility of 94% within the 0.5 ΔFMQ threshold. To calculate the propagated uncertainty, apply Eq. (2) with uncertainty values provided under Eq. (7).

5. Discussion

This chapter evaluates the performance of the applied oxybarometric systems and compares them with previous studies. A detailed discussion on the quality of the experimental approach is provided in the supplementary material (S3-quality of experiments). Further details on fitting statistics are available in supplementary material (Table S.16).

5.1. Sensitivity and robustness of geochemical oxybarometers

The previous chapter demonstrated the improved robustness of the V/Sc oxybarometer, which will now be contextualized alongside other oxybarometric systems. Vanadium-, V-Sc-, and Fe-Mg-based oxybarometers will be discussed in order of increasing complexity, with comparisons to prior experimental studies.

5.1.1. V oxybarometry

Fig. 8a compares the new data reported in this study with existing experimental data. Over a broad fO_2 range, the distribution of $\log(D_{[V]}^{[Ol/melt]})$ as a function of fO_2 is sigmoidal. The most experimental data falls within the fO_2 range FMQ -5 to +5. The values for $\log(D_{[V]}^{[Ol/melt]})$

of this study are within the range of those reported by previous studies except for a single outlier (E7.3_SB_A), previously noted in subsection 4.4.2. To evaluate the potential causes, we examine several parameters.

For example, this outlier could reflect a failure of fO_2 control, leading to redox disequilibrium. However, no Fe-Mg zoning was observed in olivine from experiment E7.3_SB_A, as confirmed by low standard errors in FeO measurements. In addition, fO_2 control was ensured by confirmed water saturation and the presence of Co and CoO_2 in the surrounding solid buffer (Table 3).

Another possibility for this shift would be an analytical artifact. LA-ICP-MS measurements on small experimentally grown olivine crystals can demonstrate difficulties due to contamination by other phases (i.e., glass matrix). If this was the case for experiment E7.3_SB_A, slight glass or spinel contaminations would be easily identified by the presence of incompatible elements in olivine (such as U) or elements characteristic of spinel (i.e., Cr). But both analytical artefacts can be ruled out (Table 5).

We infer that the degree of polymerization accounts for the outlier observed in this study. Specifically, NBO/T decreases sharply to 0.212, representing a drop of 0.173 relative to the previous step at 960 °C (where NBO/T was 0.385). In contrast, earlier temperature steps showed much smaller changes (ΔNBO/T ≤ 0.105). This decrease coincides with a pronounced reduction in V-concentration in the glass matrix to 80.3 µg/g, compared to the median value of 250.8±36.7 µg/g observed in all other experiments (Fig. 5d). Simultaneously, the corresponding olivine shows a nearly twofold increase in V-concentration (35.1 µg/g), relative to olivines from other experiments at the same fO_2 but different temperatures (V: 13.3-22.4 µg/g; T = 1019-960 °C; Table 5). This coincides with drastic increases in $\log(D_{[Sc]}^{[Ol/melt]})$ as illustrated by Fig. 5c. In fact, previous studies incorporated NBO/T as a linear factor in their V oxybarometers (Wang et al., 2019; Erdmann et al., 2024). While NBO/T will be influenced by fO_2 (i.e., through changes in the Fe^{2+}/Fe^{3+}

ratio in the silicate melt and consequently melt-polymerization) no systematic effect on the $D^{[Ol/melt]}_{[V]}$ is observed in this study.

We conclude that the observed outlier in $D^{[Ol/melt]}_{[V]}$ rises only under conditions of a pronounced change in melt polymerization, which kinetically influences the diffusion of trace elements between olivine and silicate melt (Ni et al., 2015). This is likely driven by substantial undercooling (i.e., a large temperature difference between the liquidus and the experimental run temperature). This agrees with the experimentally observed increase in relative undercooling. After the first temperature step (T = 1019 °C), the liquidus of the residual melt is experimentally constrained, so subsequent undercooling largely reflects the imposed temperature decrement. However, because the residual melt becomes increasingly evolved and viscous, even a slightly larger decrement (40 °C between 960 °C and 920 °C vs. ~30 °C in earlier steps) leads to a greater relative undercooling, enhancing kinetic effects such as diffusion-limited trace-element partitioning.

Given this outlier and to ensure robust sigmoidal regression fitting, we applied a filtering approach designed to minimize the influence of outliers while preserving asymptotic behavior. The resulting dataset (n = 167) was derived from the original 344 experiments, as detailed in Table S.17 of the supplementary material. This approach ensures that only extreme outliers are removed, affecting mostly the two endmembers of the sigmoidal curve. The resulting subset of 167 experiments was used for model calibration, while the remaining data serve as an independent test set for validation. Fig. 8b provides a closer view of the fO_2 window relevant for terrestrial systems. A linear fit is compared to the previously applied sigmoidal model. While both show similar predictive accuracy for fO_2 up to FMQ +3, the linear model offers theoretically lower parameter uncertainty and is simpler to implement, which can enhance its robustness and practical utility when used for estimating redox conditions in this range. The linear fit from Eq. (3) of this study, closely aligns with the other two regression fits. While our results for $\log(D^{[Ol/melt]}_{[V]})$ versus fO_2 align well with previous research (Canil and Fedortchouk, 2001; Mallmann and O'Neill, 2013; Shishkina et al., 2018;

Wang et al., 2019; Erdmann et al., 2024) applying our fitted models offer a twofold advancement: 1) a universal oxybarometer applicable across a broad fO_2 range; and 2) an optimized version with significantly lower prediction uncertainties tailored for hydrous melts within the relevant fO_2 window. In the following paragraph, we discuss potential sources of variance in the complete dataset to substantiate the initial data filtering approach.

The most likely reason for the variance of the data set is the influence of intensive or extensive parameters such as pressure, temperature and melt composition on $D^{[Ol/melt]}_{[V]}$. Mallmann and O'Neill (2009) observed a noticeable influence of both melt and olivine composition on the $D^{[Ol/melt]}_{[V]}$; however, Mallmann and O'Neill (2013) concluded that this effect is minimal. Regarding the effect of temperature, previous studies present conflicting conclusions: some demonstrate temperature dependence of $D^{[Ol/melt]}_{[V]}$ (Mallmann and O'Neill, 2013; Laubier et al., 2014; Wang et al., 2019; Erdmann et al., 2024) while others propose the absence or negligibility of such a relationship (Canil, 1997, 1999; Canil and Fedortchouk, 2001; Leuthold et al., 2023). Given the compositional variability of olivine and silicate melt and the wide fO_2-temperature range represented in Fig. 8a, the spread of the main dataset cannot be explained by composition or temperature alone. This variability contributes to the ~1 log unit uncertainty in $\Delta\log fO_2$ prediction, as shown in Fig. 8b. A CorMat conducted on the experimental dataset (including this study) revealed no systematic shift in predicted $\Delta\log fO_2$ as a function of temperature (see Table S.18).

Another factor could be the composition of the starting material, including its V-content. This study demonstrates that the studied melt compositional variance encompassing a large fraction of arc magmas does not yield a statistically significant effect on $D^{[Ol/melt]}_{[V]}$ (Fig. 5). In addition, Laubier et al. (2014) report that the V-content in the starting material does not influence the final V partition coefficient between olivine and silicate melt. Although most experiments are conducted under ambient pressure and anhydrous conditions, it was proposed that V partitioning is unaffected by H_2O (Shishkina et al., 2018)

and that the influence of pressure is negligible (Canil, 1997; Canil and Fedortchouk, 2001; Mallmann and O'Neill, 2013; Wang et al., 2019).

An experimental artifact could also be considered as a potential explanation. Erdmann et al. (2024) outline the challenges of achieving precise and accurate redox conditions depending on the experimental apparatus being applied (i.e., piston cylinder). Earlier, Mallmann and O'Neill (2009) noted that an observed temperature influence on V partition coefficient in case of garnet- and clinopyroxene melt pairs might result from fO_2 overestimation when using a $ReReO_2$ solid buffer. This could be explained by a detectable high standard deviation on the V partition and/or Fe-Mg exchange coefficient as a consequence of redox disequilibrium. While some variance in the dataset may arise from redox disequilibrium, as suggested by core-to-rim Fe-Mg zoning in an outlier experiment from Dygert et al. (2020), such effects are not evident in the majority of published experiments. Alternatively, these outliers and deviations may reflect incomplete attainment of kinetic equilibrium as discussed for experiment E7.3_SB_A.

Overall, using $D^{[Ol/melt]}_{[V]}$ as oxybarometer (V oxybarometer) is a powerful tool to track magmatic redox conditions. A sigmoidal regression line can be fitted to all experimental data based on the theoretical explanation of the behavior of the bulk V partitioning with changing fO_2 (Mallmann et al., 2022). The corresponding equation, where logfO_2 is expressed relative to ΔFMQ, is defined as follows:

$$\Delta FMQ = LOGx0 - \left(\log_{10}\left[4.34642 / (y + 3.11912) \right] - 1 \right) / p \quad (8)$$

with LOGx0 = -1.72333±0.0473, p = -0.09895±0.00175 and y = $D^{[Ol/melt]}_{[V]}$.

Eq. (8) demonstrates a 2σ propagated median uncertainty of 0.32 log units over the fO_2 range from ΔFMQ -5 to +5, which highly depends on the precise determination of the $D^{[Ol/melt]}_{[V]}$ and increases towards extreme fO_2 endmembers. Applying (8) on the calibrated dataset shows a success rate of reproducibility of 83% within 0.5 ΔFMQ threshold value. If

the fO_2 range is limited to FMQ -5 to +3.5, a linear fitting expression can be applied as follows:

$$\Delta FMQ = (\log(D_V^{[Ol/melt]}) + 1.34021 \pm 0.01144) / -0.23336 \pm 0.00405 \quad (9)$$

Eq. (9) demonstrates a 2σ propagated median uncertainty of 0.34 log units over the calibrated fO_2 range. It reproduces fO_2 better (88.6%) than Eq. (8) but only within the calibration range. Beyond that the linear fit leads to significant overestimation of fO_2. Note that Eq. (9) shows values for the fitting parameters similar to Eq. (3).

5.1.2. V-Sc oxybarometry

Although the V oxybarometer is well-suited to track fO_2 in magmatic systems, the previous subsection highlighted its potential sensitivity to kinetic effects. Therefore, the V oxybarometer can be improved in terms of its robustness by coupling it with the chemically similar but redox-independent Sc as demonstrated in Fig. 5b.

Comparing the V-Sc exchange coefficient between various experimental studies and with the V partition coefficient for olivine-melt pairs reveals three key differences across a broad range of fO_2: 1) The number of extreme outliers is removed (i.e., this study); 2) The offset between the trend defined by our data and those from previous studies can be attributed to differences in silicate melt NBO/T (Fig. 9a); and 3) enhanced variance of $D_{[Sc]}^{[Ol/melt]}$ for anhydrous experiments (Fig. 9b). Given the strong agreement between V-partitioning data from this and previous studies (Fig. 8) the observed offset in Fig. 9a must be linked to the olivine/melt partitioning of Sc. Fig. 9b highlights the non-linear increase of $\log(D_{[Sc]}^{[Ol/melt]})$ with decreasing temperature, whereas the V partition coefficient remains independent from temperature (Figure S.15). The variability in V partitioning is instead primarily controlled by fO_2. As silicate melt composition (e.g., NBO/T) and temperature are correlated variables in this study, it cannot be defined just based on our data which variable affects $D_{[Sc]}^{[Ol/melt]}$ more. However, statistical testing pointed out that NBO/T is a strong mediator between temperature and $D_{[Sc]}^{[Ol/melt]}$ (Figure S.16, and Tables S.14 and S.18).

Mallmann and O'Neill (2013) observed a correlation between $D_{[Sc]}^{[Ol/melt]}$ and temperature, which formed the basis of their proposed Sc-Y geothermometer. However, Mallmann and O'Neill (2013) also pointed out a noticeable effect of both melt and olivine compositions on $D_{[Sc]}^{[Ol/melt]}$. A clear correlation between NBO/T and $\log(D_{[Sc]}^{[Ol/melt]})$ might be masked by the higher variability of $D_{[Sc]}^{[Ol/melt]}$ in anhydrous experiments (Fig. 9b). Kelley and Cottrell (2012) address the limitation of the V/Sc proxy, noting that its calibration under anhydrous, atmospheric conditions may not be applicable to the high-pressure, hydrous environments of mantle wedge melting. Another possibility could be an analytical artefact for not accounting the isobaric interference of the $^{29}Si^{16}O$ signal to ^{45}Sc (subsection 3.3.1, in this study only about 1 µg/g). Although this has been corrected for in the present study and in some previous works (Mallmann and O'Neill, 2009, 2013), such interference would in a large part be canceled out during the calculation of the partition coefficient between olivine and silicate melt (Mallmann and O'Neill, 2013). This suggests that the parallel offset observed in Fig. 9a, reflects the complex behavior of $D_{[Sc]}^{[Ol/melt]}$ in response to changes in degree of melt polymerization, as illustrated in Fig. 9b. Temperature, melt composition (i.e., NBO/T), and water content all contribute to this behavior, highlighting their combined influence on diffusivity of Sc.

However, this study demonstrates that the V-Sc oxybarometer outperforms models based solely on V partitioning between olivine and silicate melt. Given the high-precision analysis of V and Sc in our setup, we recommend applying our V-Sc oxybarometer (Eq. (4)) for hydrous arc magmatic systems with NBO/T ≤ 0.6 which falls within the observed range for andesitic to basaltic rocks (Mysen et al., 1982).

5.1.3. Fe-Mg-based oxybarometry

Subsection 4.4.3. demonstrated that the $\log(K_{D[Fe_T/Mg]}^{[Ol/melt]})$ correlates with fO_2 and the corresponding equation Eq. (7) can be used as a Fe-Mg-oxybarometer within the calibrated range of this study. The Fe^{2+}-Mg exchange coefficient ($K_{D[Fe/Mg]}^{[Ol/melt]}$) between olivine and silicate

melt is known to be relatively insensitive to pressure, temperature and melt composition (Roeder and Emslie, 1970; Ford et al., 1983; Ulmer, 1989; Matzen et al., 2011; Blundy et al., 2020; Saper et al., 2022). Blundy et al. (2020) and references therein outlined the weak to negligible effect of pressure, temperature, composition and H_2O content on $K_{D[Fe/Mg]}^{[Ol/melt]}$. Despite the fact that Fe is incorporated in olivine only as ferrous iron, only a few studies considered the use of $K_{D[Fe_T/Mg]}^{[Ol/melt]}$ as oxybarometer (Roeder and Emslie, 1970; Blundy et al., 2020; Matzen et al., 2022).

Based on $K_{D[Fe/Mg]}^{[Ol/melt]}$, the measured olivine composition and MgO content in the silicate melt, we estimated the concentration of Fe(II)O in the melt, which in turn was used to calculate the Fe^{3+}/Fe_{tot} ratios in the melt by comparing it to the measured FeO_{tot} value. The values of $K_{D[Fe/Mg]}^{[Ol/melt]}$ were calculated by using the method of Toplis (2005) and Blundy et al. (2020). Fig. 10 compares the such estimated Fe^{3+}/Fe_{tot} ratios in the silicate melt with the prediction of various models (Kress and Carmichael, 1991; Jayasuriya et al., 2004; Putirka, 2016; Borisov et al., 2018).

A key observation is that the experimental dataset defines a trend parallel with the model predictions. However, the calculated values fall significantly below the predicted curves. Indeed, at our lowest experimental fO_2, negative Fe^{2+}/Fe_{tot} ratios are predicted (Fig. 10). As equilibrium has been demonstrated for our experiments, the only possible explanation for the negative values is that the model-calculated $K_{D[Fe/Mg]}^{[Ol/melt]}$ values are underestimated. Such underestimation would yield a systematic shift of our dataset to lower Fe^{2+}/Fe^{3+} independently of fO_2, which is consistent with the observation in Fig. 10. Indeed, if we increased the value of $K_{D[Fe/Mg]}^{[Ol/melt]}$ by ~25 rel.% the calculated Fe^{2+}/Fe_{tot} ratios are consistent with the model predictions. Such an offset is plausible as the calibration dataset of Toplis (2005) and Blundy et al. (2020) is dominated by data from experiments conducted at significantly higher temperature ($T \geq 1025$ C) and with predominantly more mafic melt

compositions. In fact, Blundy et al. (2020) addressed limitations in their calibrations, particularly for melts with ~60 wt.% SiO_2.

Overall, we conclude that the $\log(K_{D[Fe_T/Mg]}^{[Ol/melt]})$ can serve as an oxybarometer (for fO_2 > ~FMQ -0.5) in experimental studies, providing reliable fO_2 estimates under controlled conditions. When the composition of the silicate melt in equilibrium with the olivine can be determined, it may also be useful for field-based research, where a rapid shift in redox conditions may be effectively recorded by diffusive Fe-Mg exchange between olivine and silicate melt (Shea et al., 2023). In contrast, V-based oxybarometers, which are less affected by diffusion, preserve the original magmatic fO_2 recorded by melt inclusions (Canil, 1997, 2002; Anser Li and Aeolus Lee, 2004). Thus, combining these approaches offers complementary insights into both the initial and evolving redox conditions in natural magmatic systems.

5.2. Comparison of oxybarometers

To evaluate the performance of V-based oxybarometers under experimental conditions, Fig. 11 uses the dataset from subsection 4.4.2 to compare calculated fO_2 values with those determined experimentally. This comparison covers a large proportion of that being relevant for terrestrial systems (Mallmann et al., 2022). For a quantitative comparison of accuracy and precision of each oxybarometer, Fig. 12 demonstrates the corresponding concordance correlation coefficients (CCC, Fig. 12a), 2σ propagated uncertainty (Unc., Fig. 12b) and root mean square error (RMSE, Fig. 12c). Since the oxybarometers of this study are calibrated using the entire dataset of this study such a high CCC-value is expected. To strengthen the evaluation, we included a comparison of the best-performing oxybarometers from this study using an extended dataset, alongside the top-performing model from previous studies. This allows the evaluation of potential overfitting and provides a robust test for the practical applicability of the oxybarometer.

All oxybarometers of this study show very good performance (CCC > 0.9) accompanied by low RMSE values. The Fe-Mg-oxybarometer (Eq. (7)) demonstrates the highest uncertainty

(2σ, ~1 ΔFMQ), while V-Sc oxybarometer performs at best regarding all parameters combined (CCC = 0.93, RMSE = 0.252, 2σ-Unc. ~0.41 ΔFMQ). The oxybarometers of Erdmann et al. (2024) and Shishkina et al. (2018) are comparable in their performance with CCC around 0.85. Only the oxybarometers of Wang et al. (2019) and Mallmann and O'Neill (2013) display a similar systematic overestimation of the measured fO_2 (Fig. 11). Consequently, both reveal lower CCC values (CCC < 0.6), higher RMSE and propagated uncertainties (2σ, > 1 ΔFMQ). The first published oxybarometer by Canil and Fedortchouk (2001) shows an almost equally good performance as oxybarometers of this study. As the V-Sc oxybarometer (Eq. (2)) is only calibrated within the constraints of this study, we compare the most promising V oxybarometers of this study (Eqs. (8) and (3)) with the one from Canil and Fedortchouk (2001) on an extended dataset (n = 345). All three show elevated RMSE compared to their application on the small dataset (n = 31, this study) but comparable CCC and propagated uncertainty values. V oxybarometer of Eq. (8) demonstrates the best performance (CCC > 0.9 and 2σ-Unc. ~0.5 ΔFMQ). It reflects its advantage to be more precise and accurate for very oxidizing conditions (> FMQ +3.5), where a linear regression fits to systematic overestimation of fO_2.

Overall, the V-based oxybarometers of this study offering low calibration uncertainties (2σ-Unc. < 0.5 ΔFMQ), high precision and accuracy along with flexibility and robustness across a wide *P*-*T*-*X*-fO_2 space. Nevertheless, the V-Sc oxybarometer displays the best performance (i.e., robustness) within the calibration range (NBO/T ≤ 0.6) of this study and offers a high precision oxybarometer for olivine-bearing hydrous basaltic-andesitic magmatic systems, typically found at convergent plate boundaries.

6. Implications

As olivine is a common phenocryst in hydrous basaltic to andesitic magmas in volcanic arcs, the oxybarometers proposed in this study will facilitate improved reconstruction of the redox evolution of arc magmatic systems. They will allow to reconstruct the initial fO_2 of primitive magmas and potential redox changes during early stages of magma differentiation with high precision and accuracy (2σ < 0.4 ΔFMQ) independent of melt composition. This, in

turn, will enhance our understanding of magma genesis, the role of fO_2 in controlling volatile speciation, metal transport capacity, and its influence on volcanic degassing.

We recommend the following procedure to apply $D_{[V]}^{[Ol/melt]}$ and $K_{D[V/Sc]}^{[Ol/melt]}$ as oxybarometers to enhance accuracy and precision:

(1) Initial calculation: Use Eq. (8) $\left[fO_2(\Delta FMQ) = f_{sig}\left(\log(D_V^{[Ol/melt]})\right)\right]$ to estimate the fO_2.

(2) Validation and cross-check: If the calculated fO_2 falls within a range of FMQ -5 to FMQ +3.5, apply Eq. (3) $\left[fO_2(\Delta FMQ) = f_{lin}\left(\log(D_V^{[Ol/melt]})\right)\right]$.

(3) If NBO/T ≤ 0.6 (NBO/T calculated following Eq. (3) from Zajacz and Tsay (2019), which is based on the formulation of Mysen and Richet (2005)): Apply Eq. (4) $\left[fO_2(\Delta FMQ) = f_{lin}\left(\log(K_{D[V/Sc]}^{[Ol/melt]})\right)\right]$ to estimate the fO_2 with higher accuracy than in step (1).

Importantly, better redox constraints also help assess the fertility of distinct magma series such as calc-alkaline, shoshonitic, and even adakitic, which are associated with different tectonic settings and ore deposit types (Sillitoe, 2010; Wilkinson, 2013; Richards, 2015; Chen and Wu, 2020; Chiaradia, 2021; Heinrich, 2024). Future applications should focus on silicate melt inclusions from both mineralized and barren systems to better constrain the links between magma redox state, tectonic setting, and ore fertility of magmatic-hydrothermal systems.

7. Conclusions

V partitioning between olivine and silicate melt serves as a reliable proxy for tracking and quantifying redox changes in magmatic environments. This study bridges theoretical understanding (i.e., Mallmann et al., 2022) and empirical calibration of V-based oxybarometry in olivine silicate melt systems by integrating new complementary experimental data with most available literature data by using statistical analysis. Through precise and adaptable fO_2 control and refined LA-ICP-MS measurements on small olivine

crystals, this study extends our quantitative understanding of the fO_2 dependence of V and Sc partitioning and Fe-Mg exchange between olivine and silicate melt to low-temperature (T = 920-1019 °C) hydrous systems and tests the effect of silicate melt composition. We have demonstrated the systematic independence of V partitioning between olivine and silicate melt from intensive parameters (P-T-X and aH_2O). The remaining variance in V partitioning reflects the precision and accuracy of experimental fO_2 control and may additionally derive from potential analytical uncertainties and disruptions in the kinetic equilibrium between olivine and silicate melt. The latter may be related to melt structure, though the link to polymerization (e.g., NBO/T) remains tentative and may instead reflect effects of undercooling in a few low-temperature experiments (T ~920 °C). Coupling the $D^{[Ol/melt]}_{[V]}$ with redox-independent Sc partitioning compensates for this phenomenon improving robustness and accuracy of reconstructing fO_2 but only within the calibrated range of this study (i.e., NBO/T ≤ 0.6). Thus, we propose optimized V-based oxybarometers primarily in the range of logfO_2 from FMQ -5 to FMQ +5 encompassing the relevant magmatic redox conditions within the Earth system. The best of these is based on $D^{[Ol/melt]}_{[V]}$ and yields a 2σ uncertainty of < 0.33 log units on fO_2 estimation. Specifically, for magmatic arc systems with fO_2 = FMQ -1 to FMQ +3.5, $K_{D[V/Sc]}^{[Ol/melt]}$ demonstrates a comparable 2σ uncertainty of < 0.41 log units, and it shows enhanced robustness against kinetic effects if applied within calibration range of this study (i.e., NBO/T ≤ 0.6). In addition, it will help gain new insights into the role of magmatism and volcanic degassing in the redox evolution of the Earth's crust and atmosphere.

Acknowledgments

We would like to thank Michael Schirra, Stefan Farsang, and Agathe Martignier from the University of Geneva for their assistance with LA-ICP-MS, Raman Spectroscopy, and SEM. Special thanks are due to Florence Begue, and Charline Lormand for providing training on the EPMA instrumentation. We are also deeply grateful to Frederic Arlaud for his technical support across various laboratories. We are grateful to Edwin Gnos from the Natural History

Museum in Geneva for granting mineral standards and Wim Malfait from Empa Material Science and Technology for invaluable instructions to prepare synthetic alkali silicate glasses. Additionally, we would like to acknowledge Zsofia Palos, Mara Miranda, Sophie Webb, Corin Jorgenson, Alessandro Musu, Martin Miranda Muruzabal, Alex Cugerone, and Frank Förster for their insightful discussions and feedback on the model calculations. This project has received funding from the European Research Council (ERC) under the European Union's Horizon 2020 research and innovation program (grant agreement no. 864792), ERC Consolidator Grant OXYGEN , awarded to Zoltán Zajacz.

CRediT authorship contribution statement

Enzo-Enrico Cacciatore: Writing – original draft, Visualization, Validation, Software, Project administration, Methodology, Investigation, Formal analysis, Data curation, Conceptualization. **Zoltán Zajacz**: Writing – review and editing, Validation, Supervision, Project administration, Resources, Methodology, Funding acquisition, Conceptualization. **Alexandra Tsay**: Methodology, Writing – review and editing and Resources. **Ivano Gennaro**: Software. **Kalin Kouzmanov**: Methodology and Writing – review and editing.

Data availability

Data are available through Mendeley Data online at https://doi.org/10.17632/78jwj86xgd.1.

Appendix A. Supplementary material

The supplementary material includes the following: 1) S1_Supplementary_Tables, 2) S2_Supplement_Quality_of_experimental_approach, 3) S3_Supplementary_Figures, and 4) S4_Supplement_AI_generated_Python_Codes.

S1: Excel tables with LA-ICP-MS, EPMA, and QEMSCAN analysis, as well as numerical data for statistical modeling (correlation matrix, fitting statistics, etc.) and coding input.

S2: Details on the quality of experiments.

S3: Figures illustrating precision and accuracy of EPMA and LA-ICP-MS measurements, along with statistical modeling.

S4: AI-generated Python code.

Supplementary material is available online at https://doi.org/10.17632/78jwj86xgd.1.

Declaration of Generative AI and AI-assisted technologies in the writing process

During the preparation of this work, the authors used OpenAI's ChatGPT (Mar 14 version) to assist in generating Python code related to Equations Eq. (5), and (6). After using this tool, the authors reviewed and edited the content as needed and take full responsibility for the content of the publication.

References

Aeolous Lee, C.-T., Leeman, W.P., Canil, D., Li, Z.-X.A., 2005. Similar V/Sc Systematics in MORB and Arc Basalts: Implications for the Oxygen Fugacities of their Mantle Source Regions. Journal of Petrology 46(11), 2313-2336. https://doi.org/10.1093/petrology/egi056.

Ai, Y., Chiaradia, M., Wu, C., Chen, H., 2024. Crustal magma oxidation state and endowments in porphyry copper deposits. Science China Earth Sciences. https://doi.org/10.1007/s11430-024-1429-6.

Alex, A., Zajacz, Z., 2020. A new method to quantitatively control oxygen fugacity in externally heated pressure vessel experiments. European Journal of Mineralogy 32(1), 219-234. https://doi.org/10.5194/ejm-32-219-2020.

Alex, A., Zajacz, Z., 2022. A new high-pressure experimental apparatus to study magmatic processes at precisely controlled redox conditions. American Mineralogist 107(4), 692-702. https://doi.org/10.2138/am-2022-7977.

Anser Li, Z.-X., Aeolus Lee, C.-T., 2004. The constancy of upper mantle fO2 through time inferred from V/Sc ratios in basalts. Earth and Planetary Science Letters 228(3), 483-493. https://doi.org/10.1016/j.epsl.2004.10.006.

Arató, R., Audétat, A., 2017. Experimental calibration of a new oxybarometer for silicic magmas based on vanadium partitioning between magnetite and silicate melt. Geochimica et Cosmochimica Acta 209, 284-295. https://doi.org/10.1016/j.gca.2017.04.020.

Ballhaus, C., Berry, R.F., Green, D.H., 1991. High pressure experimental calibration of the olivine-orthopyroxene-spinel oxygen geobarometer: implications for the oxidation state of the upper mantle. Contributions to Mineralogy and Petrology 107(1), 27-40. https://doi.org/10.1007/BF00311183.

Blundy, J., Melekhova, E., Ziberna, L., Humphreys, M.C.S., Cerantola, V., Brooker, R.A., McCammon, C.A., Pichavant, M., Ulmer, P., 2020. Effect of redox on Fe–Mg–Mn exchange between olivine and melt and an oxybarometer for basalts. Contributions to Mineralogy and Petrology 175(11), 103-103. https://doi.org/10.1007/s00410-020-01736-7.

Borisov, A., Behrens, H., Holtz, F., 2018. Ferric/ferrous ratio in silicate melts: a new model for 1 atm data with special emphasis on the effects of melt composition. Contributions to Mineralogy and Petrology 173(12), 98-98. https://doi.org/10.1007/s00410-018-1524-8.

Botcharnikov, R.E., Holtz, F., Behrens, H., 2015. Solubility and fluid–melt partitioning of H2O and Cl in andesitic magmas as a function of pressure between 50 and 500MPa. Chemical Geology 418, 117-131. https://doi.org/10.1016/j.chemgeo.2015.07.019.

Brounce, M., Kelley, K.A., Cottrell, E., Reagan, M.K., 2015. Temporal evolution of mantle wedge oxygen fugacity during subduction initiation. Geology 43(9), 775-778. https://doi.org/10.1130/G36742.1.

Bucholz, C.E., Kelemen, P.B., 2019. Oxygen fugacity at the base of the Talkeetna arc, Alaska. Contributions to Mineralogy and Petrology 174(10), 79-79. https://doi.org/10.1007/s00410-019-1609-z.

Burgisser, A., Scaillet, B., 2007. Redox evolution of a degassing magma rising to the surface. Nature 445(7124), 194-197. https://doi.org/10.1038/nature05509.

Burnham, A.D., Mallmann, G., Fonseca, R.O.C., 2020. Mineral-melt partitioning of redox-sensitive elements. Earth and Space Science Open Archive. https://doi.org/10.1002/essoar.10503118.1.

Canil, D., 1997. Vanadium partitioning and the oxidation state of Archaean komatiite magmas. Nature 389(6653), 842-845. https://doi.org/10.1038/39860.

Canil, D., 1999. Vanadium partitioning between orthopyroxene, spinel and silicate melt and the redox states of mantle source regions for primary magmas. Geochimica et Cosmochimica Acta 63(3), 557-572. https://doi.org/10.1016/S0016-7037(98)00287-7.

Canil, D., 2002. Vanadium in peridotites, mantle redox and tectonic environments: Archean to present. Earth and Planetary Science Letters 195(1), 75-90. https://doi.org/10.1016/S0012-821X(01)00582-9.

Canil, D., Fedortchouk, Y., 2001. Olivine-liquid partitioning of Vanadium and other trace elements, with applications to modern and ancient picrites. The Canadian Mineralogist 39(2), 319-330. https://doi.org/10.2113/gscanmin.39.2.319.

Carmichael, I.S.E., 1991. The redox states of basic and silicic magmas: a reflection of their source regions? Contributions to Mineralogy and Petrology 106(2), 129-141. https://doi.org/10.1007/BF00306429.

Carmichael, I.S.E., Ghiorso, M.S., 1990. The effect of oxygen fugacity on the redox state of natural liquids and their crystallizing phases. Reviews in Mineralogy and Geochemistry 24(1), 191-212. https://doi.org/10.1515/9781501508769-011.

Chen, H., Wu, C., 2020. Metallogenesis and major challenges of porphyry copper systems above subduction zones. Science China Earth Sciences 63(7), 899-918. https://doi.org/10.1007/s11430-019-9595-8.

Chiaradia, M., 2014. Copper enrichment in arc magmas controlled by overriding plate thickness. Nature Geoscience 7(1), 43-46. https://doi.org/10.1038/ngeo2028.

Chiaradia, M., 2021. Magmatic controls on metal endowments of porphyry Cu-Au deposits. In: Tectonomagmatic Influences on Metallogeny and Hydrothermal Ore Deposits: A Tribute to Jeremy P. Richards, Society of Economic Geologists. pp. 1-16. https://doi.org/10.5382/SP.24.01.

Churakov, S.V., Gottschalk, M., 2003. Perturbation theory based equation of state for polar molecular fluids: I. Pure fluids. Geochimica et Cosmochimica Acta 67(13), 2397-2414. https://doi.org/10.1016/S0016-7037(02)01347-9.

Cicconi, M.R., Moretti, R., Neuville, D.R., Guest, E., 2020. Redox Engine of Earth. Elements: An International Magazine of Mineralogy, Geochemistry, and Petrology 16(3), 148-220.

Cottrell, E., Birner, S., Brounce, M., Davis, F., Waters, L., Kelley, K., 2021. Oxygen Fugacity Across Tectonic Settings. Earth and Space Science Open Archive, 61-61. https://doi.org/10.1002/essoar.10502445.1.

da Silva, M.M., Holtz, F., Namur, O., 2017. Crystallization experiments in rhyolitic systems: The effect of temperature cycling and starting material on crystal size distribution. American Mineralogist 102(11), 2284-2294. https://doi.org/10.2138/am-2017-5981.

Dygert, N., Draper, D.S., Rapp, J.F., Lapen, T.J., Fagan, A.L., Neal, C.R., 2020. Experimental determinations of trace element partitioning between plagioclase, pigeonite, olivine, and lunar basaltic melts and an fO2 dependent model for plagioclase-melt Eu partitioning. Geochimica et Cosmochimica Acta 279, 258-280. https://doi.org/10.1016/j.gca.2020.03.037.

Earthchem Portal, 2021. EarthChem Database. https://www.earthchem.org/.

Ehlers, K., Grove, T.L., Sisson, T.W., Recca, S.I., Zervas, D.A., 1992. The effect of oxygen fugacity on the partitioning of nickel and cobalt between olivine, silicate melt, and metal. Geochimica et Cosmochimica Acta 56(10), 3733-3743. https://doi.org/10.1016/0016-7037(92)90166-G.

Erdmann, S., Pichavant, M., Gaillard, F., 2024. Mineral-melt vanadium oxybarometry for primitive arc magmas: effect of hydrous melt composition on fO2 estimates. Contributions to Mineralogy and Petrology 179(4), 39-39. https://doi.org/10.1007/s00410-024-02113-4.

Eugster, H.P., 1957. Heterogeneous reactions involving oxidation and reduction at high pressures and temperatures. The Journal of Chemical Physics 26(6), 1760-1761. https://doi.org/10.1063/1.1743626.

Evans, K.A., 2012. The redox budget of subduction zones. Earth-Science Reviews 113(1), 11-32. https://doi.org/10.1016/j.earscirev.2012.03.003.

Farsang, S., Zajacz, Z., 2025. Sulfur species and gold transport in arc magmatic fluids. Nature Geoscience. https://doi.org/10.1038/s41561-024-01601-3.

Ford, C.E., Russell, D.G., Craven, J.A., Fisk, M.R., 1983. Olivine-Liquid Equilibria: Temperature, Pressure and Composition Dependence of the Crystal/Liquid Cation Partition Coefficients for Mg, Fe2+, Ca and Mn. Journal of Petrology 24(3), 256-266. https://doi.org/10.1093/petrology/24.3.256.

Frost, B.R., 1991. Chapter 1. Introduction to oxygen fugacity and its petrologic importance, in: Lindsley, D.H. (Ed.) Oxide Minerals: Petrologic and Magnetic Significance. De Gruyter, Berlin, Boston, pp. 1-10. https://doi.org/10.1515/9781501508684-004.

Gaetani, G.A., Grove, T.L., 1997. Partitioning of moderately siderophile elements among olivine, silicate melt, and sulfide melt: Constraints on core formation in the Earth and Mars. Geochimica et Cosmochimica Acta 61(9), 1829-1846. https://doi.org/10.1016/S0016-7037(97)00033-1.

Gavrilenko, M., Batanova, V.G., Llovet, X., Krasheninnikov, S., Koshlyakova, A.N., Sobolev, A.V., 2023. Secondary fluorescence effect quantification of EPMA analyses of olivine grains embedded in basaltic glass. Chemical Geology 621, 121328-121328. https://doi.org/10.1016/j.chemgeo.2023.121328.

Gorman, J.K., Nardella, W.R., 1962. Hydrogen permeation through metals. Vacuum 12(1), 19-24. https://doi.org/10.1016/0042-207X(62)90821-7.

Guillong, M., Meier, D.L., Allan, M.M., Heinrich, C.A., Yardley, B.W.D., 2008. Appendix A6: SILLS: A MATLAB-based program for the reduction of laser ablation ICP-MS data of homogeneous materials and inclusions. Mineralogical Association of Canada Short Course 40, 328-333. https://doi.org/10.3749/9780921294801.app06.

Gunter, W.D., Myers, J., Wood, J.R., 1979. The Shaw bomb, an ideal hydrogen sensor. Contributions to Mineralogy and Petrology 70(1), 23-27. https://doi.org/10.1007/BF00371868.

Heinrich, C.A., 2024. The Chain of Processes Forming Porphyry Copper Deposits—An Invited Paper*. Economic Geology 119(4), 741-769. https://doi.org/10.5382/econgeo.5069.

Hewitt, D.A., 1977. Hydrogen fugacities in Shaw bomb experiments. Contributions to Mineralogy and Petrology 65(2), 165-169. https://doi.org/10.1007/BF00371056.

Jayasuriya, K.D., O'Neill, H.S.C., Berry, A.J., Campbell, S.J., 2004. A Mössbauer study of the oxidation state of Fe in silicate melts. American Mineralogist 89(11-12), 1597-1609. https://doi.org/10.2138/am-2004-11-1203.

Jenner, F.E., O'Neill, H.S.C., 2012. Major and trace analysis of basaltic glasses by laser-ablation ICP-MS. Geochemistry, Geophysics, Geosystems 13(3), n/a-n/a. https://doi.org/10.1029/2011GC003890.

Kelley, K.A., Cottrell, E., 2012. The influence of magmatic differentiation on the oxidation state of Fe in a basaltic arc magma. Earth and Planetary Science Letters 329-330, 109-121. https://doi.org/10.1016/j.epsl.2012.02.010.

Kress, V.C., Carmichael, I.S.E., 1991. The compressibility of silicate liquids containing Fe2O3 and the effect of composition, temperature, oxygen fugacity and pressure on their redox states. Contributions to Mineralogy and Petrology 108(1), 82-92. https://doi.org/10.1007/BF00307328.

Lanari, P., Vho, A., Bovay, T., Airaghi, L., Centrella, S., 2019. Quantitative compositional mapping of mineral phases by electron probe micro-analyser. Geological Society, London, Special Publications 478(1), 39-63. https://doi.org/10.1144/SP478.4.

Lanari, P., Vidal, O., De Andrade, V., Dubacq, B., Lewin, E., Grosch, E.G., Schwartz, S., 2014. XMapTools: A MATLAB©-based program for electron microprobe X-ray image processing and geothermobarometry. Computers & Geosciences 62, 227-240. https://doi.org/10.1016/j.cageo.2013.08.010.

Laubier, M., Grove, T.L., Langmuir, C.H., 2014. Trace element mineral/melt partitioning for basaltic and basaltic andesitic melts: An experimental and laser ICP-MS study with application to the oxidation state of mantle source regions. Earth and Planetary Science Letters 392, 265-278. https://doi.org/10.1016/j.epsl.2014.01.053.

Lawrence, I.K.L., 1989. A Concordance Correlation Coefficient to Evaluate Reproducibility. Biometrics 45(1), 255-268. https://doi.org/10.2307/2532051.

Lee, C.-T.A., Luffi, P., Chin, E.J., Bouchet, R., Dasgupta, R., Morton, D.M., Le Roux, V., Yin, Q.-z., Jin, D., 2012. Copper Systematics in Arc Magmas and Implications for Crust-Mantle Differentiation. Science 336(6077), 64 LP-68. https://doi.org/10.1126/science.1217313.

Lee, C.-T.A., Luffi, P., Le Roux, V., Dasgupta, R., Albaréde, F., Leeman, W.P., 2010. The redox state of arc mantle using Zn/Fe systematics. Nature 468(7324), 681-685. https://doi.org/10.1038/nature09617.

Lesne, P., Scaillet, B., Pichavant, M., Iacono-Marziano, G., Beny, J.-M., 2011. The H2O solubility of alkali basaltic melts: an experimental study. Contributions to Mineralogy and Petrology 162(1), 133-151. https://doi.org/10.1007/s00410-010-0588-x.

Leuthold, J., Blundy, J., Ulmer, P., 2023. Trace element partitioning in basaltic systems as a function of oxygen fugacity. Contributions to Mineralogy and Petrology 178(12), 95-95. https://doi.org/10.1007/s00410-023-02069-x.

Longerich, H.P., Jackson, S.E., Günther, D., 1996. Inter-laboratory note. Laser ablation inductively coupled plasma mass spectrometric transient signal data acquisition and analyte concentration calculation. Journal of Analytical Atomic Spectrometry 11(9), 899-904. https://doi.org/10.1039/JA9961100899.

Mallmann, G., Burnham, A.D., Fonseca, R.O.C., 2022. Mineral-Melt Partitioning of Redox-Sensitive Elements, Magma Redox Geochemistry. pp. 345-367. https://doi.org/10.1002/9781119473206.ch17.

Mallmann, G., O'Neill, H.S.C., 2009. The Crystal/Melt Partitioning of V during Mantle Melting as a Function of Oxygen Fugacity Compared with some other Elements (Al, P, Ca, Sc, Ti, Cr, Fe, Ga, Y, Zr and Nb). Journal of Petrology 50(9), 1765-1794. https://doi.org/10.1093/petrology/egp053.

Mallmann, G., O'Neill, H.S.C., 2013. Calibration of an Empirical Thermometer and Oxybarometer based on the Partitioning of Sc, Y and V between Olivine and Silicate Melt. Journal of Petrology 54(5), 933-949. https://doi.org/10.1093/petrology/egt001.

Marquardt, D.W., 1963. An Algorithm for Least-Squares Estimation of Nonlinear Parameters. Journal of the Society for Industrial and Applied Mathematics 11(2), 431-441. https://doi.org/10.1137/0111030.

Marxer, F., Ulmer, P., Müntener, O., 2021. Polybaric fractional crystallisation of arc magmas: an experimental study simulating trans-crustal magmatic systems. Contributions to Mineralogy and Petrology 177(1), 3-3. https://doi.org/10.1007/s00410-021-01856-8.

Matzen, A.K., Baker, M.B., Beckett, J.R., Stolper, E.M., 2011. Fe–Mg Partitioning between Olivine and High-magnesian Melts and the Nature of Hawaiian Parental Liquids. Journal of Petrology 52(7-8), 1243-1263. https://doi.org/10.1093/petrology/egq089.

Matzen, A.K., Woodland, A., Beckett, J.R., Wood, B.J., 2022. Oxidation state of iron and Fe-Mg partitioning between olivine and basaltic martian melts. 107(7), 1442-1452. https://doi.org/doi:10.2138/am-2021-7682.

Métrich, N., 2022. Redox State of Volatiles and Their Relationships with Iron in Silicate Melts, Magma Redox Geochemistry. pp. 215-232. https://doi.org/10.1002/9781119473206.ch11.

Moré, J.J., 1978. The Levenberg-Marquardt algorithm: Implementation and theory, in: Watson, G.A. (Ed.) Numerical Analysis. Springer Berlin Heidelberg, Berlin, Heidelberg, pp. 105-116. https://doi.org/10.1007/BFb0067700.

Moretti, R., Neuville, D.R., 2022. Redox Equilibria, Magma Redox Geochemistry. pp. 1-17. https://doi.org/10.1002/9781119473206.ch1.

Moretti, R., Ottonello, G., 2022. Silicate Melt Thermochemistry and the Redox State of Magmas. Reviews in Mineralogy and Geochemistry 87(1), 339-403. https://doi.org/10.2138/rmg.2022.87.08.

Motulsky, H., Christopoulos, A., 2004. Fitting Models to Biological Data Using Linear and Nonlinear Regression: A practical guide to curve fitting. Oxford University Press. https://doi.org/10.1093/oso/9780195171792.001.0001.

Muan, A., Osborn, E.F., 1956. Phase Equilibria at Liquidus Temperatures in the System MgO-FeO-Fe2O3-SiO2. Journal of the American Ceramic Society 39(4), 121-140. https://doi.org/10.1111/j.1151-2916.1956.tb14178.x.

Mysen, B.O., 2006. Redox equilibria of iron and silicate melt structure: Implications for olivine/melt element partitioning. Geochimica et Cosmochimica Acta 70(12), 3121-3138. https://doi.org/10.1016/j.gca.2006.03.014.

Mysen, B.O., Richet, P., 2005. Silicate Glasses and Melts: Properties and Structure. Elsevier, Amsterdam, Boston, London, New York, Oxford, Paris, San Diego, San Francisco, Singapore, Sydney, Tokyo. https://doi.org/10.1016/S0921-3198(05)X8001-2.

Mysen, B.O., Virgo, D., Seifert, F.A., 1982. The structure of silicate melts: Implications for chemical and physical properties of natural magma. Reviews of Geophysics 20(3), 353-383. https://doi.org/10.1029/RG020i003p00353.

Nandedkar, R.H., 2014. Thesis: Evolution of hydrous mantle-derived calc-alkaline liquids by fractional crystallization at 0.7 and 0.4 GPa: An experimental study. ETH Zurich.

Nandedkar, R.H., Ulmer, P., Müntener, O., 2014. Fractional crystallization of primitive, hydrous arc magmas: an experimental study at 0.7 GPa. Contributions to Mineralogy and Petrology 167(6), 1015-1015. https://doi.org/10.1007/s00410-014-1015-5.

Ni, H., Hui, H., Steinle-Neumann, G., 2015. Transport properties of silicate melts. Reviews of Geophysics 53(3), 715-744. https://doi.org/10.1002/2015RG000485.

OriginLab, 2024. OriginPro (Version 2024 Academic) OriginLab Corporation.

Osborn, E.F., 1959. Role of oxygen pressure in the crystallization and differentiation of basaltic magma. American Journal of Science 257(9), 609 LP-647. https://doi.org/10.2475/ajs.257.9.609.

Papike, J.J., Burger, P.V., Bell, A.S., Le, L., Shearer, C.K., Sutton, S.R., Jones, J., Newville, M., 2013. Developing vanadium valence state oxybarometers (spinel-melt, olivine-melt, spinel-olivine) and V/(Cr+Al) partitioning (spinel-melt) for martian olivine-phyric basalts. American Mineralogist 98(11-12), 2193-2196. https://doi.org/10.2138/am.2013.4622.

Park, J.-W., Campbell, I.H., Chiaradia, M., Hao, H., Lee, C.-T., 2021. Crustal magmatic controls on the formation of porphyry copper deposits. Nature Reviews Earth & Environment 2(8), 542-557. https://doi.org/10.1038/s43017-021-00182-8.

Paton, C., Hellstrom, J., Paul, B., Woodhead, J., Hergt, J., 2011. Iolite: Freeware for the visualisation and processing of mass spectrometric data. Journal of Analytical Atomic Spectrometry 26(12), 2508-2518. https://doi.org/10.1039/C1JA10172B.

Pirrie, D., Butcher, A.R., Power, M.R., Gottlieb, P., Miller, G.L., 2004. Rapid quantitative mineral and phase analysis using automated scanning electron microscopy (QemSCAN); potential applications in forensic geoscience, in: Pye, K., Croft, D.J. (Eds.), Forensic Geoscience: Principles, Techniques and Applications. Geological Society of London, p. 0. https://doi.org/10.1144/gsl.Sp.2004.232.01.12.

Putirka, K., 2016. Rates and styles of planetary cooling on Earth, Moon, Mars, and Vesta, using new models for oxygen fugacity, ferric-ferrous ratios, olivine-liquid Fe-Mg exchange, and mantle potential temperature. American Mineralogist 101(4), 819-840. https://doi.org/10.2138/am-2016-5402.

Rauchenstein-Martinek, K., Wagner, T., Wälle, M., Heinrich, C.A., 2014. Gold concentrations in metamorphic fluids: A LA-ICPMS study of fluid inclusions from the Alpine orogenic belt. Chemical Geology 385, 70-83. https://doi.org/10.1016/j.chemgeo.2014.07.018.

Richards, J.P., 2015. The oxidation state, and sulfur and Cu contents of arc magmas: implications for metallogeny. Lithos 233, 27-45. https://doi.org/10.1016/j.lithos.2014.12.011.

Roeder, P.L., Emslie, R.F., 1970. Olivine-Liquid Equilibrium. Contributions to Mineralogy and Petrology, 29 (4): 275-289.

Saper, L.M., Baker, M.B., Stolper, E.M., 2022. Fe2+–Mg partitioning between olivine and liquid at low oxygen fugacity: an experimental and thermodynamic framework. Contributions to Mineralogy and Petrology 177(10), 94-94. https://doi.org/10.1007/s00410-022-01955-0.

Sato, M., 1978. Oxygen fugacity of basaltic magmas and the role of gas-forming elements. Geophysical Research Letters 5(6), 447-449. https://doi.org/10.1029/GL005i006p00447.

Scaillet, B., Pichavant, M., Roux, J., Humbert, G., Lefevre, A., 1992. Improvements of the Shaw membrane technique for measurement and control of fH2 at high temperatures and pressures. American Mineralogist 77(5-6), 647-655.

Schindelin, J., Arganda-Carreras, I., Frise, E., Kaynig, V., Longair, M., Pietzsch, T., Preibisch, S., Rueden, C., Saalfeld, S., Schmid, B., Tinevez, J.-Y., White, D.J., Hartenstein, V., Eliceiri, K., Tomancak, P., Cardona, A., 2012. Fiji: an open-source platform for biological-image analysis. Nature Methods 9(7), 676-682. https://doi.org/10.1038/nmeth.2019.

Shaw, H.R., 1963. Hydrogen-Water Vapor Mixtures: Control of Hydrothermal Atmospheres by Hydrogen Osmosis. Science 139(3560), 1220 LP-1222. https://doi.org/10.1126/science.139.3560.1220.

Shea, T., Ruth, D., Jollands, M., Ohtaki, K., Ishii, H., Bradley, J., 2023. The presence of silicate melt may enhance rates of cation diffusion in olivine. Earth and Planetary Science Letters 621, 118370. https://doi.org/10.1016/j.epsl.2023.118370.

Shearer, C.K., McKay, G., Papike, J.J., Karner, J.M., 2006. Valence state partitioning of vanadium between olivine-liquid: Estimates of the oxygen fugacity of Y980459 and application to other olivine-phyric martian basalts. American Mineralogist 91(10), 1657-1663. https://doi.org/10.2138/am.2006.2155.

Shishkina, T.A., Portnyagin, M.V., Botcharnikov, R.E., Almeev, R.R., Simonyan, A.V., Garbe-Schönberg, D., Schuth, S., Oeser, M., Holtz, F., 2018. Experimental calibration and implications of olivine-melt vanadium oxybarometry for hydrous basaltic arc magmas. American Mineralogist 103(3), 369-383. https://doi.org/10.2138/am-2018-6210.

Sillitoe, R.H., 2010. Porphyry copper systems. Economic Geology 105(1), 3-41. https://doi.org/10.2113/gsecongeo.105.1.3.

Stanley, C.R., Lawie, D., 2007. Average Relative Error in Geochemical Determinations: Clarification, Calculation, and a Plea for Consistency. Exploration and Mining Geology 16(3-4), 267-275. https://doi.org/10.2113/gsemg.16.3-4.267.

Tang, M., Erdman, M., Eldridge, G., Lee, C.-T.A., 2018. The redox “filter” beneath magmatic orogens and the formation of continental crust. Science Advances 4(5). https://doi.org/10.1126/sciadv.aar4444.

Tassara, S., Reich, M., Cannatelli, C., Konecke, B.A., Kausel, D., Morata, D., Barra, F., Simon, A.C., Fiege, A., Morgado, E., Leisen, M., 2020. Post-melting oxidation of highly primitive basalts from the southern Andes. Geochimica et Cosmochimica Acta 273, 291-312. https://doi.org/10.1016/j.gca.2020.01.042.

Toplis, M.J., 2005. The thermodynamics of iron and magnesium partitioning between olivine and liquid: criteria for assessing and predicting equilibrium in natural and experimental systems. Contributions to Mineralogy and Petrology 149(1), 22-39. https://doi.org/10.1007/s00410-004-0629-4.

Tuff, J., O’Neill, H.S.C., 2010. The effect of sulfur on the partitioning of Ni and other first-row transition elements between olivine and silicate melt. Geochimica et Cosmochimica Acta 74(21), 6180-6205. https://doi.org/10.1016/j.gca.2010.08.014.

Ulmer, P., 1989. The dependence of the Fe2+-Mg cation-partitioning between olivine and basaltic liquid on pressure, temperature and composition. Contributions to Mineralogy and Petrology 101(3), 261-273. https://doi.org/10.1007/BF00375311.

van Gerve, T.D., Namur, O., 2023. SilicH2O: a graphical user interface for processing silicate glass Raman spectra and quantifying H2O. Volcanica 6(2), 405–413. https://doi.org/10.30909/vol.06.02.405413.

Wang, J., Xiong, X., Takahashi, E., Zhang, L., Li, L., Liu, X., 2019. Oxidation State of Arc Mantle Revealed by Partitioning of V, Sc, and Ti Between Mantle Minerals and Basaltic Melts. Journal of Geophysical Research: Solid Earth 124(5), 4617-4638. https://doi.org/10.1029/2018JB016731.

Wilkinson, J.J., 2013. Triggers for the formation of porphyry ore deposits in magmatic arcs. Nature Geoscience 6(11), 917-925. https://doi.org/10.1038/ngeo1940.

Zajacz, Z., Candela, P.A., Piccoli, P.M., Sanchez-Valle, C., 2012. The partitioning of sulfur and chlorine between andesite melts and magmatic volatiles and the exchange coefficients of major cations. Geochimica et Cosmochimica Acta 89, 81-101. https://doi.org/10.1016/j.gca.2012.04.039.

Zajacz, Z., Halter, W., Malfait, W.J., Bachmann, O., Bodnar, R.J., Hirschmann, M.M., Mandeville, C.W., Morizet, Y., Müntener, O., Ulmer, P., Webster, J.D., 2005. A composition-independent quantitative determination of the water content in silicate glasses and silicate melt inclusions by confocal Raman spectroscopy. Contributions to Mineralogy and Petrology 150(6), 631-642. https://doi.org/10.1007/s00410-005-0040-9.

Zajacz, Z., Seo, J.H., Candela, P.A., Piccoli, P.M., Tossell, J.A., 2011. The solubility of copper in high-temperature magmatic vapors: A quest for the significance of various chloride and sulfide complexes. Geochimica et Cosmochimica Acta 75(10), 2811-2827. https://doi.org/10.1016/j.gca.2011.02.029.

Zajacz, Z., Tsay, A., 2019. An accurate model to predict sulfur concentration at anhydrite saturation in silicate melts. Geochimica et Cosmochimica Acta 261, 288-304. https://doi.org/10.1016/j.gca.2019.07.007.

Zanetti, A., Tiepolo, M., Oberti, R., Vannucci, R., 2004. Trace-element partitioning in olivine: modelling of a complete data set from a synthetic hydrous basanite melt. Lithos 75(1), 39-54. https://doi.org/10.1016/j.lithos.2003.12.022.

Zhao, S.-Y., Yang, A.Y., Langmuir, C.H., Zhao, T.-P., 2022. Oxidized primary arc magmas: Constraints from Cu/Zr systematics in global arc volcanics. Science Advances 8(12), eabk0718-eabk0718. https://doi.org/10.1126/sciadv.abk0718.

Figure captions

Fig. 1. An example of LA-ICP-MS analysis of olivines. a) Typical ablation scenarios: 1) pure olivine ablation until glass matrix is reached underneath; 2) contamination of the ablation by a spinel inclusion; and 3) irregularities of olivine's geometry in depth lead to early contamination of the signal by the silicate glass matrix. b) Typical LA-ICP-MS signal of olivine showing scenario 2 with spinel inclusion and the onset of glass ablation. c) Backscattered electron (BSE) image of the laser pit in olivine.

Fig. 2. Time series experiments reflecting Ol-melt equilibrium via a) $\log(K_{D[Fe_T/Mg]}^{[Ol/melt]})$ and b) $\log(K_{D[V/Sc]}^{[Ol/melt]})$. The time series was carried out at fO_2 ~FMQ +2.5, T = 960 °C.

Fig. 3. Iron intensity distribution maps (WDX-EPMA) in olivines for representative samples (a) E1.1_IV_A (fO_2 = FMQ +3.56, T = 990 °C) and (b) E7.0_II_SB_A (fO_2 = FMQ -0.87, T = 1019 °C). From left to right BSE-image and Fe-map are displayed with relative intensities denoted by the accompanying color bar, demonstrating consistent chemical homogeneity. The bright rim visible between the glass matrix and the olivine is due to the topographic contrast effects. Mineral abbreviations: olivine (Ol), plagioclase (Pl) and spinel (Spl).

Fig. 4. Experimental run products of the MKCA series of the E7.X_SB-fO_2-LLD (~FMQ -1) shown in BSE-images. Olivine is present in addition to a variety of other mineral phases. Mineral abbreviations as in Fig. 3. Additional abbreviations: amphibole, (Amp), apatite (Ap), clinopyroxene (Cpx), glass (Gl), ilmenite (Ilm), and orthopyroxene (Opx).

Fig. 5. Summary of the behavior of V and Sc as a function of logfO_2 in olivine and silicate melt. a) to d): $\log(D_{[V]}^{[Ol/melt]})$, $\log(K_{D[V/Sc]}^{[Ol/melt]})$, $\log(D_{[Sc]}^{[Ol/melt]})$ and V-content as a function of logfO_2 (ΔFMQ), respectively. For all fits: $p < 0.0001$. In a) and b) linear fitting was applied. Experiment E7.3_SB_A is considered as an outlier with respect to the $\log(D_{[V]}^{[Ol/melt]})$ and therefore excluded from the linear regression in panel (a). The quality of the fit is expressed by high coefficient of determination (R^2) and very low root mean squared error (RMSE) values. b) to d): Symbol rims are color coded depending on the degree of polymerization expressed via the ratio of nonbridging oxygen per tetrahedrally coordinated cations (NBO/T). Liner fit (purple line) in panel (a) with fixed intercept derived from exploratory fitting on $D_{[V]}^{[Ol/melt]}$ as a function of fO_2 revealed the best fitting equation (for further details see supplementary material S1).

Fig. 6. Summary of the behavior of Fe and Mg as a function of logfO_2 in olivine and silicate melt. a) and b): The $\log(K_{D[Fe_T/Mg]}^{[Ol/melt]})$ versus logfO_2(ΔFMQ) with sigmoidal fitting. For all fits: $p < 0.0001$. a): Comparison of multiple sigmoidal fitting for subset of data: 1) only MKCA 2) only SHOSH 3) all combined 4) all combined except of significant outliers (*). b) Display of modeled Fe-Mg exchange coefficient between olivine and melt ($\log(K_{D[Fe_T/Mg]}^{[Ol/melt]})_{mod}$) based on NBO/T and molar fraction of fayalite in olivine (X_{Fay}). For further details, see the main text. d) and c): FeO and MgO (in olivine and glass) as a function of logfO_2(ΔFMQ), respectively.

Fig. 7. Corrected Fe-Mg exchange coefficient between olivine and melt ($\log(K_{D[Fe_T/Mg]}^{[Ol/melt]})cor$) as a function of logfO_2. The applied sigmoidal regression line ($p < 0.0001$) serves as a Fe-Mg-oxybarometer for olivine silicate melt pairs, as defined by Eq. (7).

Fig. 8. Comparison of $\log(D_{[V]}^{[Ol/melt]})$ from published and current study data (TS, this study) as a function of logfO_2. For all fits: $p < 0.0001$. a) Sigmoidal fit to the pre-filtered data (see supplement Table S.17 for details on data filtering, Outliers* marked by elliptical circles). b) Relevant distribution of V partitioning for terrestrial redox system. A comparison between linear fitting (blue, n = 149) and sigmoidal fitting (red, n = 167) from panel (a) is presented. The pink dashed-dotted line derives from linear regression fit from Eq. (3). Source of previous experimental data: Canil, 1997, 1999; Gaetani and Grove, 1997; Canil and Fedortchouk, 2001; Zanetti et al., 2004; Mallmann and O'Neill, 2009, 2013; Tuff and O'Neill, 2010; Papike et al., 2013; Laubier et al., 2014; Shishkina et al., 2018; Wang et al., 2019; Dygert et al., 2020; Leuthold et al., 2023; Erdmann et al., 2024.

Fig. 9. Comparison of $\log(K_{D[V/Sc]}^{[Ol/melt]})$ and $\log(D_{[Sc]}^{[Ol/melt]})$ from published and current study data as a function of logfO_2 and temperature, respectively. For all fits: $p < 0.0001$ a) Sigmoidal fit to the pre-filtered data (see supplement Table S.17 for details on data filtering, Outliers* marked by elliptical circles). Apparent is a parallel offset for experiments of this study at very low NBO/T values. b) Accounting for the effect of NBO/T on $\log(D_{[Sc]}^{[Ol/melt]})$ while capturing its temperature influence, the $\log(D_{[Sc]}^{[Ol/melt]})$ demonstrates moderate exponential increase with decreasing temperature and NBO/T. Note increased scattering for anhydrous experiments. For further details, see the main text. Source of previous (V-Sc) experimental data: Canil and Fedortchouk, 2001; Zanetti et al., 2004; Mallmann and O'Neill, 2009, 2013; Tuff and O'Neill, 2010; Laubier et al., 2014; Shishkina et al., 2018; Wang et al., 2019; Dygert et al., 2020; Leuthold et al., 2023; Erdmann et al., 2024. Sigmoidal fit through dataset from this study including fixed asymptote values based (horizontal dashed blue lines) on an apparent parallel shift compared to previous experiment at higher NBO/T values.

Fig. 10. Comparison of calculated Fe^{3+}/Fe_{tot} ratios in silicate melt derived from the $\log(K_{D[Fe/Mg]}^{[Ol/melt]})$ in this study with values predicted by different empirical models. The Fe^{3+}/Fe_{tot} ratios were calculated using the K_D-models of Toplis (2005) and Blundy et al. (2020). Uncertainties on these calculated Fe^{3+}/Fe_{tot} ratios are based on the 1σ calibration uncertainty in K_D (±0.03 for both models) combined with error propagation from calculated exchange coefficient and analytical uncertainties on Fe and Mg concentrations in both olivine and glass. The pink dashed line indicates a ratio value of zero. Predicted values are shown as lines derived from the empirical models (Kress and Carmichael, 1991; Jayasuriya et al., 2004; Putirka, 2016; Borisov et al., 2018). Literature (Lit.) values used as input for these prediction models correspond to the same experiments shown in Fig. 8, but with Fe-Mg-exchange data obtained from the original experimental studies.

Fig. 11. Accuracy and precision assessment of existing Ol-melt oxybarometers. Comparison between measured and calculated logfO_2 (both expressed as ΔFMQ). Vertical error bars represent 1σ propagated uncertainty based on analytical uncertainties (i.e., V- and Sc- concentrations) and errors of the fitting parameters except for studies where an equation was given to calculate the errors as 1σ (Shishkina et al. 2018; Erdmann et al. 2024). 1) Dataset includes all experiments of this study with except for outlier E7.3_SB_A (n = 31). 2) Existing V-based oxybarometers were tested from previous studies (Canil and Fedortchouk, 2001; Mallmann and O'Neill, 2013; Shishkina et al., 2018; Wang et al., 2019; Erdmann et al., 2024). 3) The most promising oxybarometers were applied on an extended experimental dataset (FMQ -5 to +5, n = 345) to evaluate potential overfitting.

Fig. 12. Statistical comparison of different olivine-melt oxybarometers presented in Fig. 11. a) Quantitative assessment of each oxybarometer's precision and accuracy using the concordance correlation coefficient (CCC). For more details see the main text. b) RMSE values for each linear fit. c) Median uncertainty (2σ) when applying each oxybarometer to its respective dataset. Superscripts correspond to those in Fig. 11.

This manuscript is a **non-peer-reviewed preprint**. A **substantially revised and peer-reviewed version** has been published in: *Geochimica et Cosmochimica Acta*
https://doi.org/10.1016/j.gca.2025.12.025

Figures

Figure 1

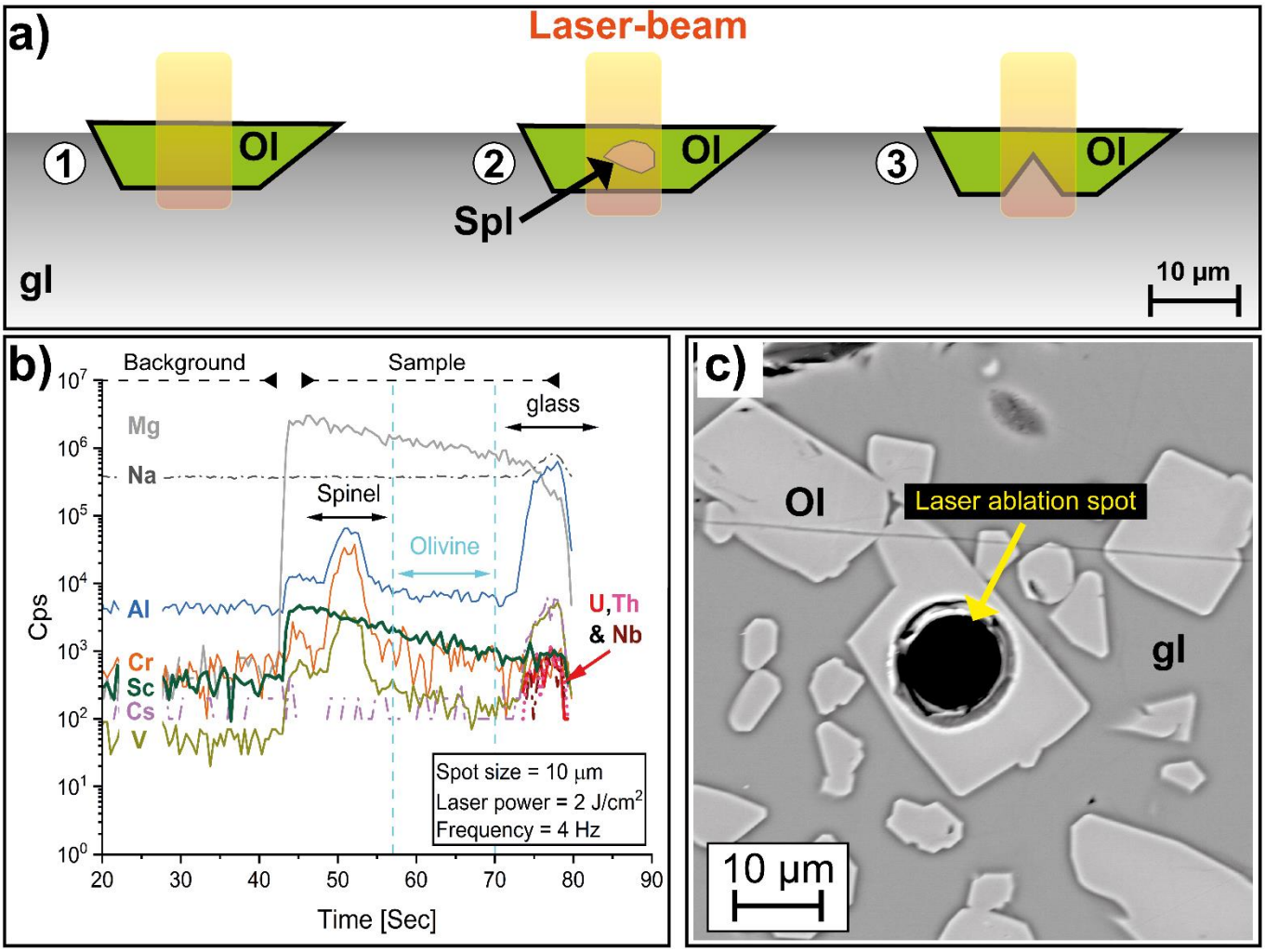

Figure 2

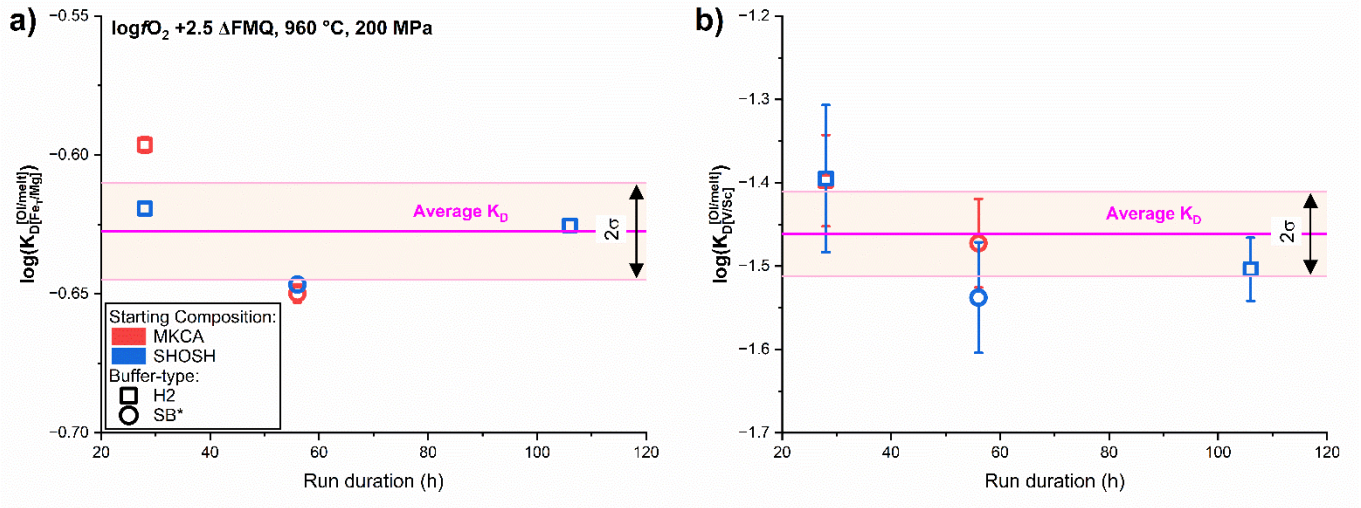

This manuscript is a **non-peer-reviewed preprint**. A **substantially revised and peer-reviewed version** has been published in: *Geochimica et Cosmochimica Acta*
https://doi.org/10.1016/j.gca.2025.12.025

Figure 3

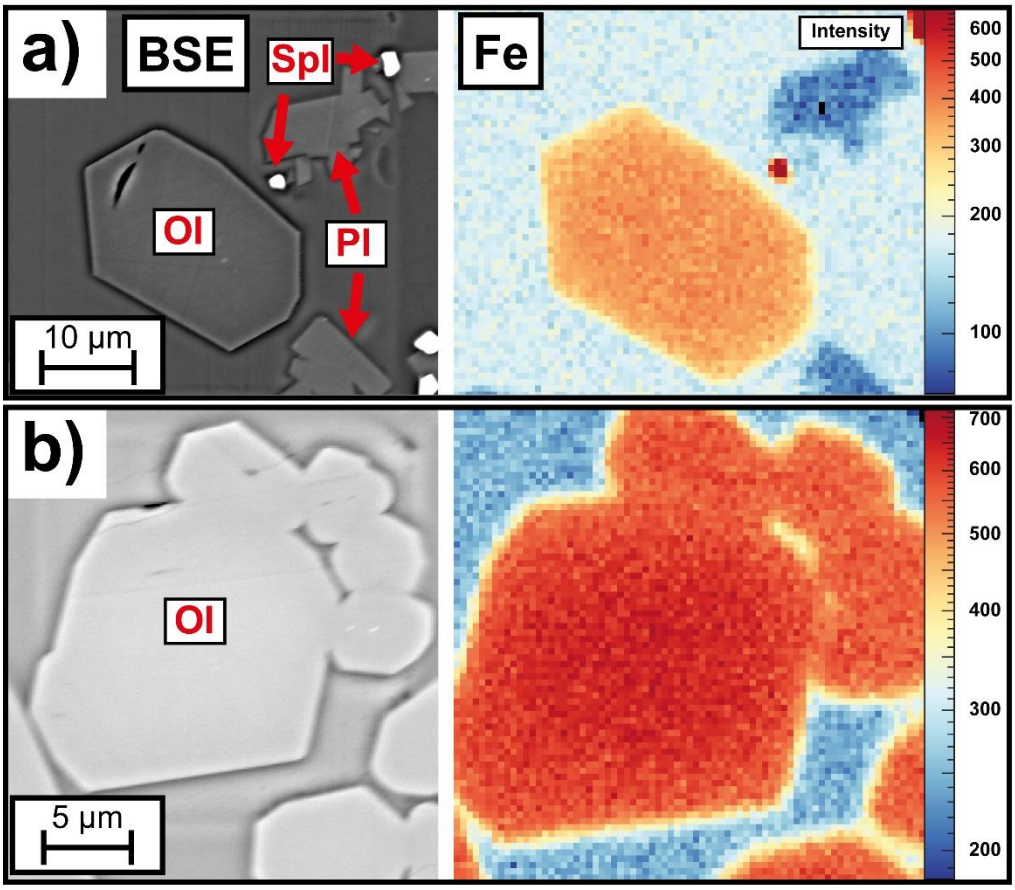

This manuscript is a **non-peer-reviewed preprint**. A **substantially revised and peer-reviewed version** has been published in: *Geochimica et Cosmochimica Acta*
https://doi.org/10.1016/j.gca.2025.12.025

Figure 4

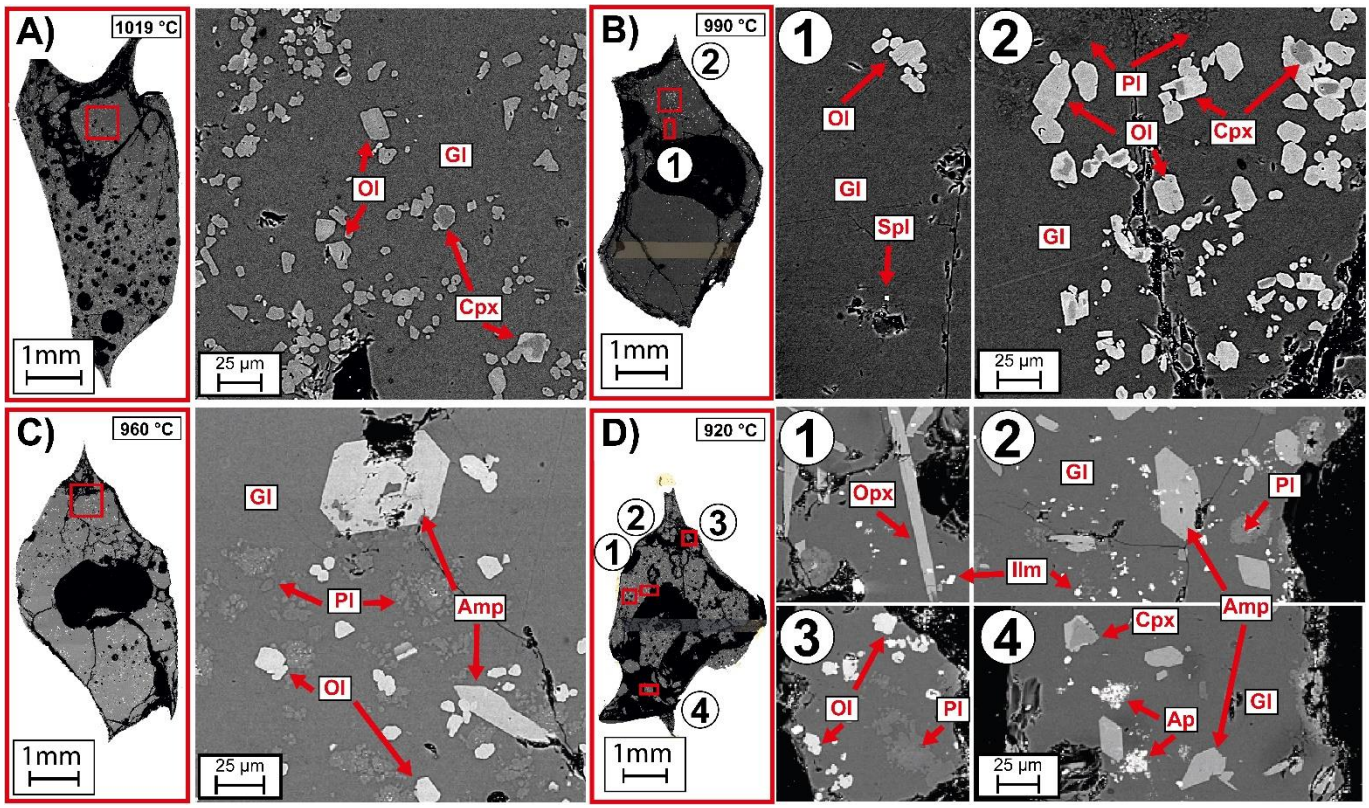

This manuscript is a **non-peer-reviewed preprint**. A **substantially revised and peer-reviewed version** has been published in: *Geochimica et Cosmochimica Acta*
https://doi.org/10.1016/j.gca.2025.12.025

Figure 5

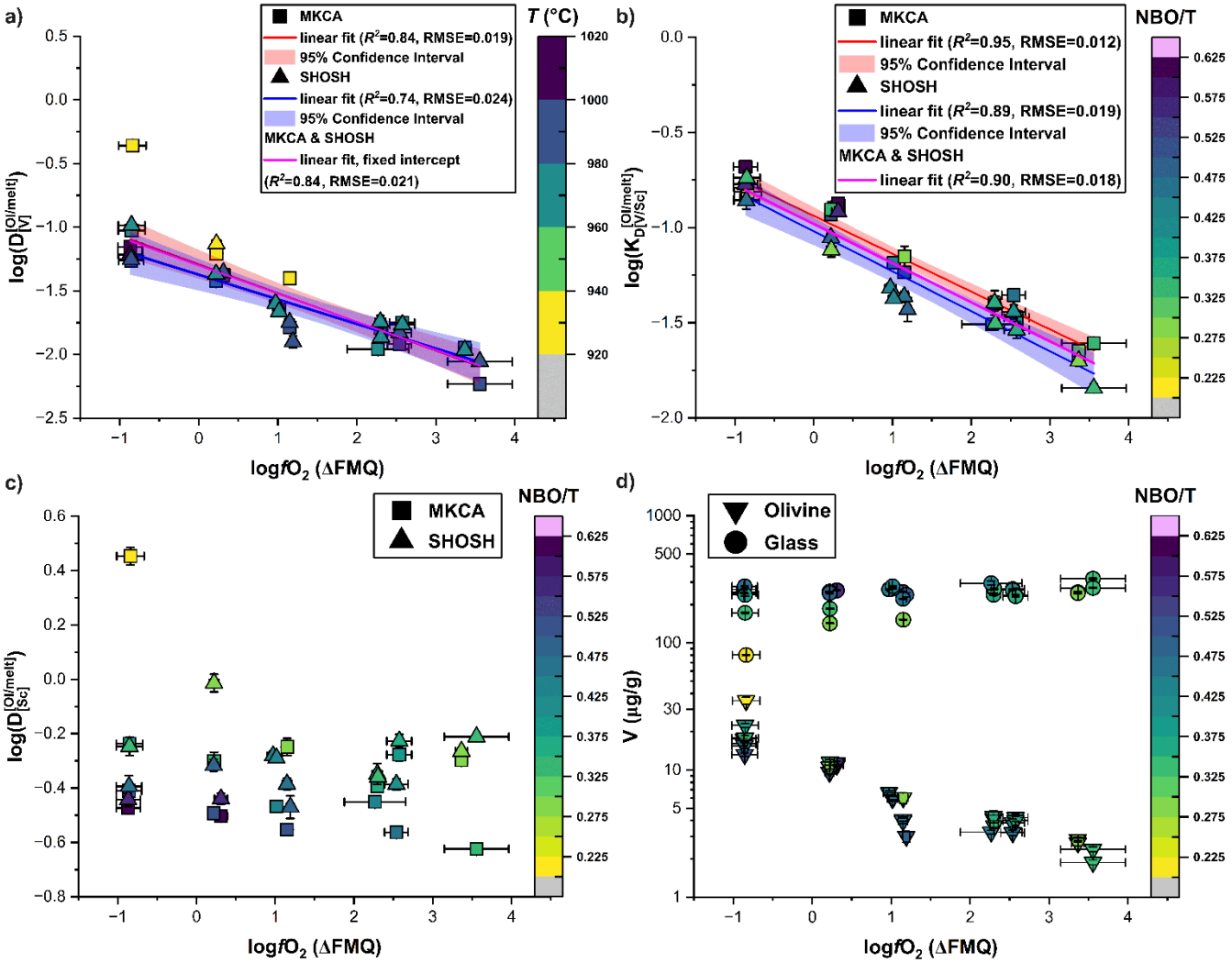

This manuscript is a **non-peer-reviewed preprint**. A **substantially revised and peer-reviewed version** has been published in: *Geochimica et Cosmochimica Acta*
https://doi.org/10.1016/j.gca.2025.12.025

Figure 6

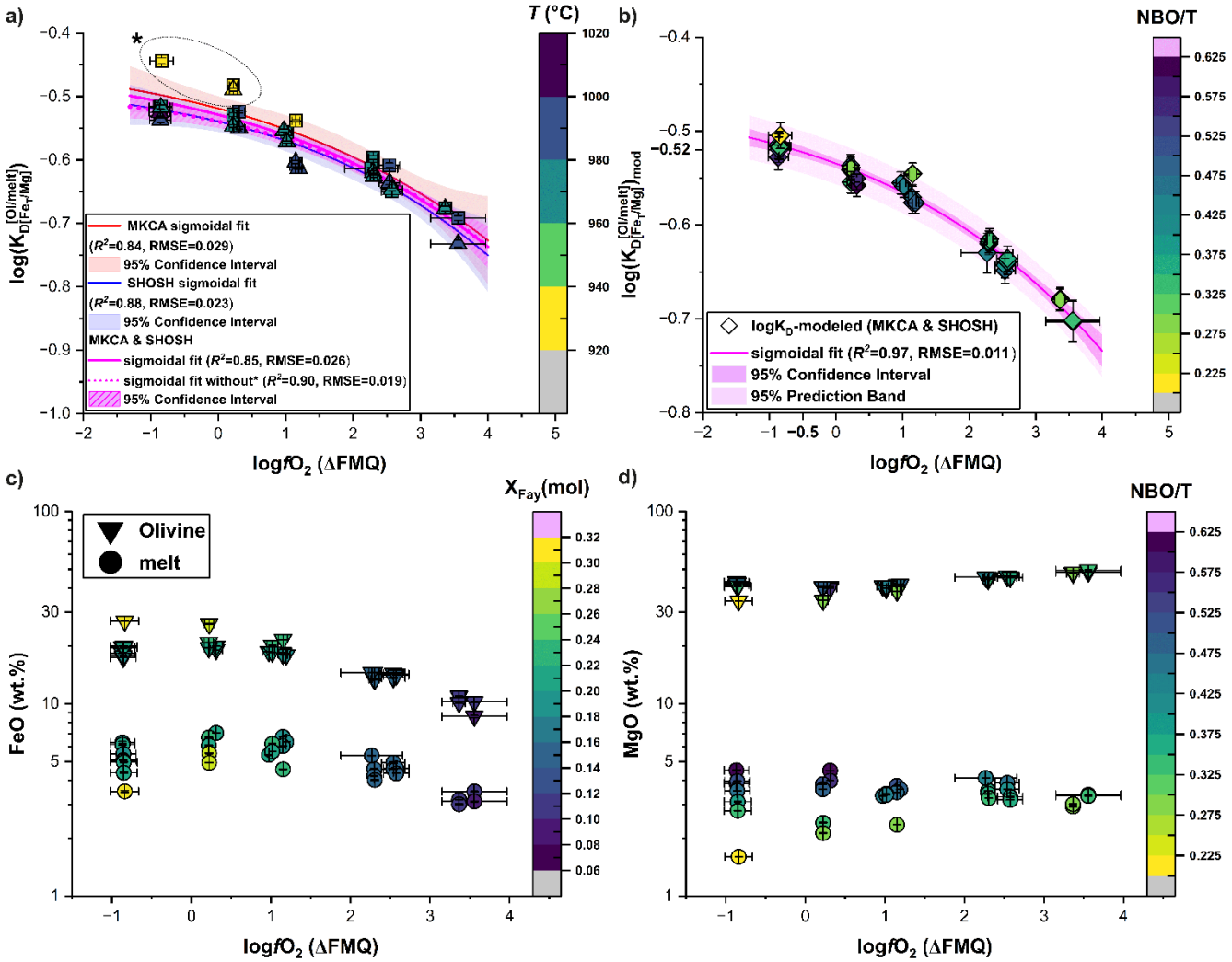

This manuscript is a **non-peer-reviewed preprint**. A **substantially revised and peer-reviewed version** has been published in: *Geochimica et Cosmochimica Acta*
https://doi.org/10.1016/j.gca.2025.12.025

Figure 7

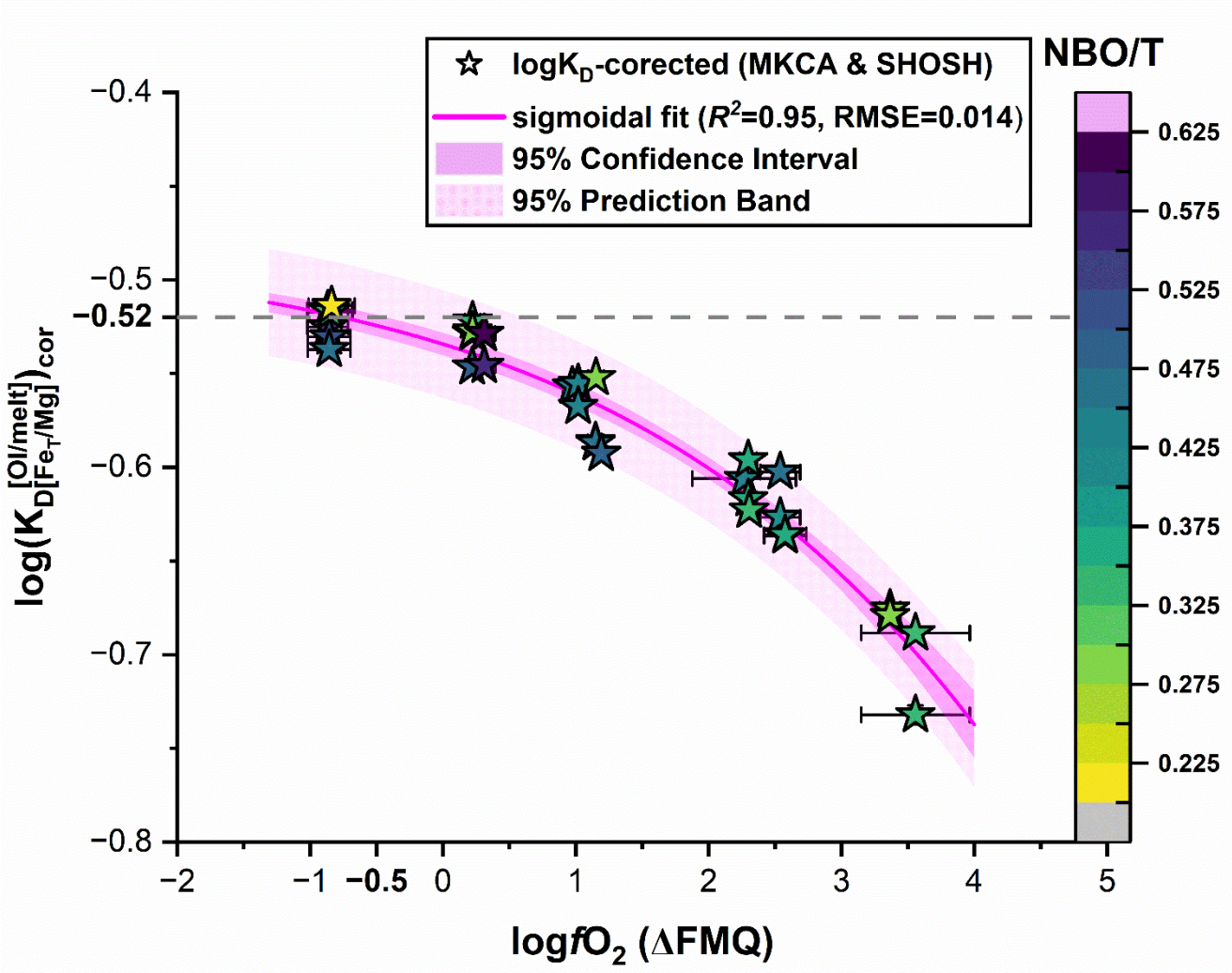

Figure 8

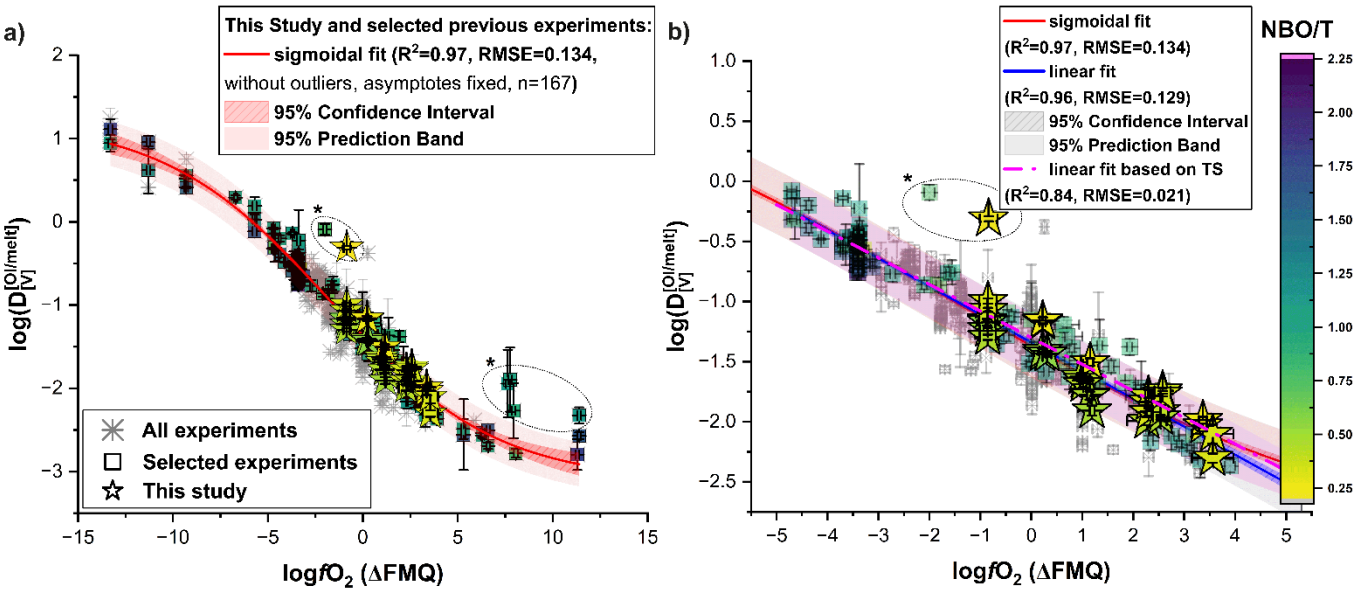

This manuscript is a **non-peer-reviewed preprint**. A **substantially revised and peer-reviewed version** has been published in: *Geochimica et Cosmochimica Acta*
https://doi.org/10.1016/j.gca.2025.12.025

Figure 9

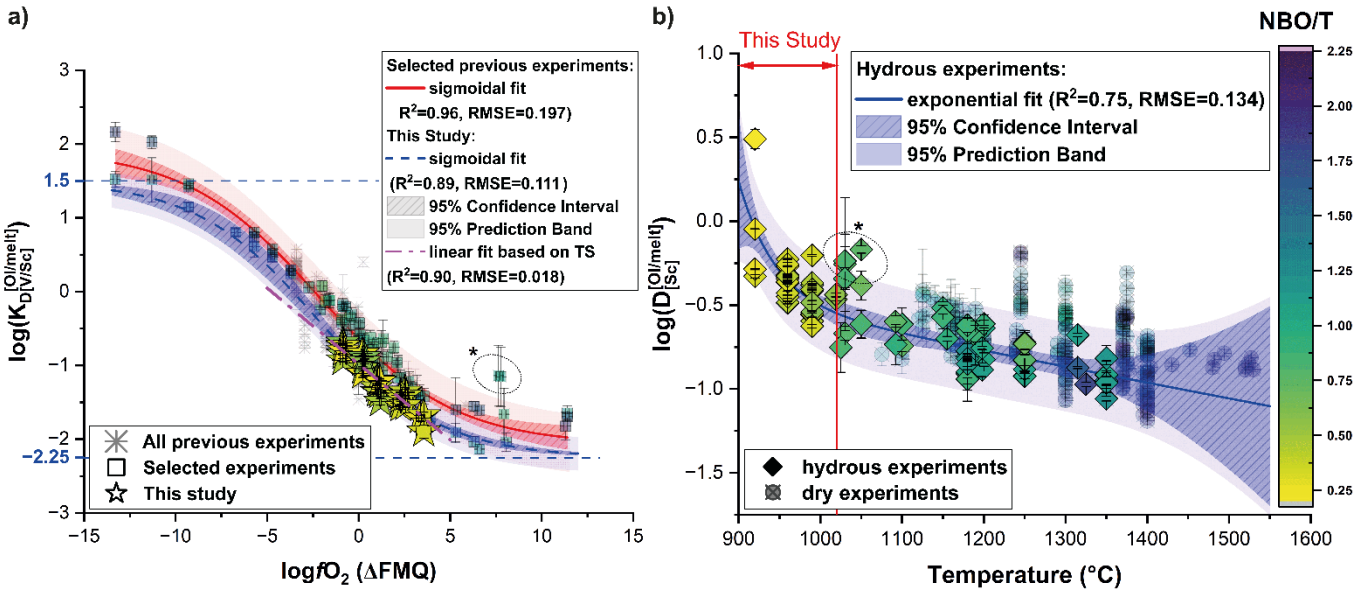

Figure 10

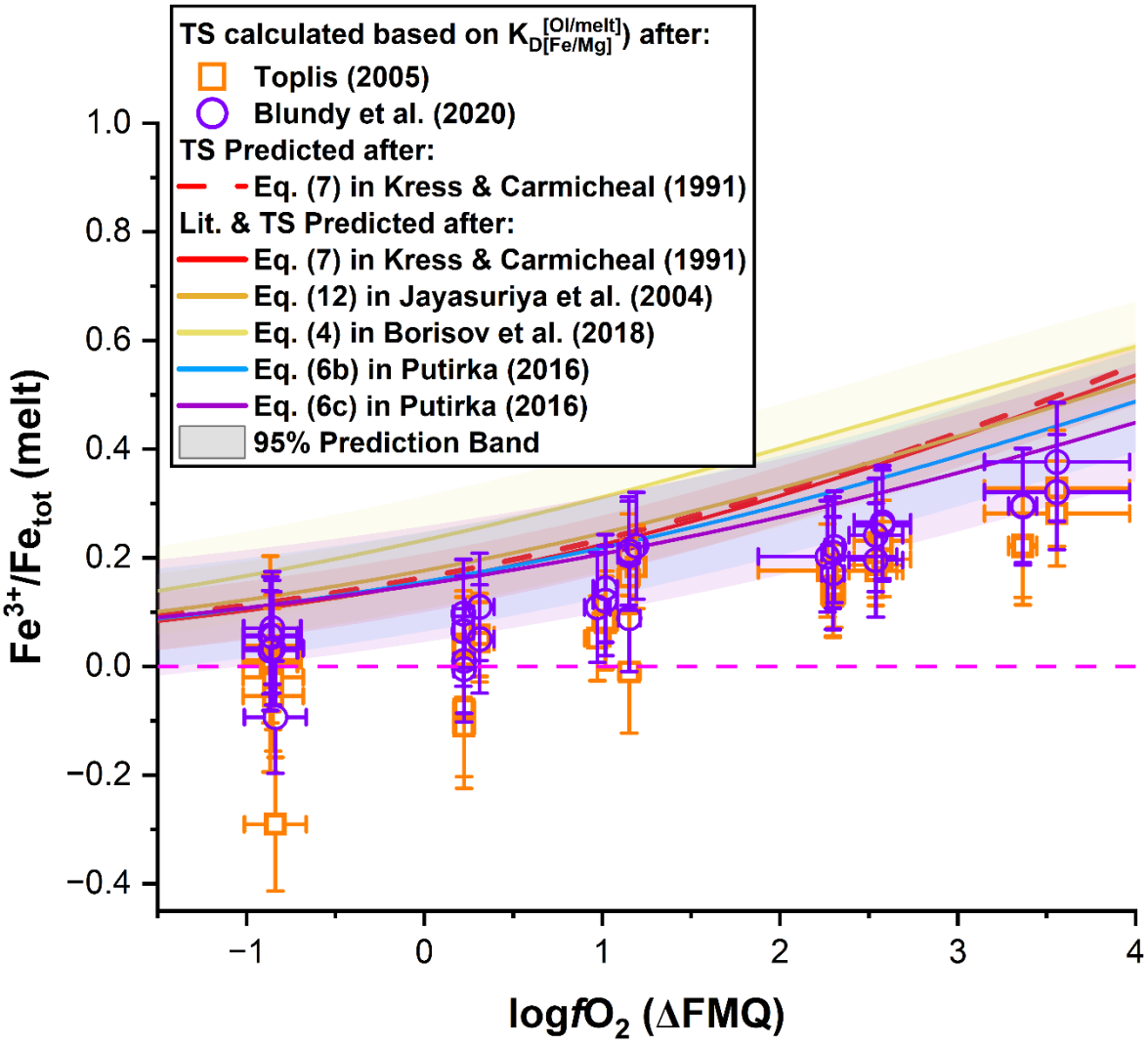

This manuscript is a **non-peer-reviewed preprint**. A **substantially revised and peer-reviewed version** has been published in: *Geochimica et Cosmochimica Acta*
https://doi.org/10.1016/j.gca.2025.12.025

Figure 11

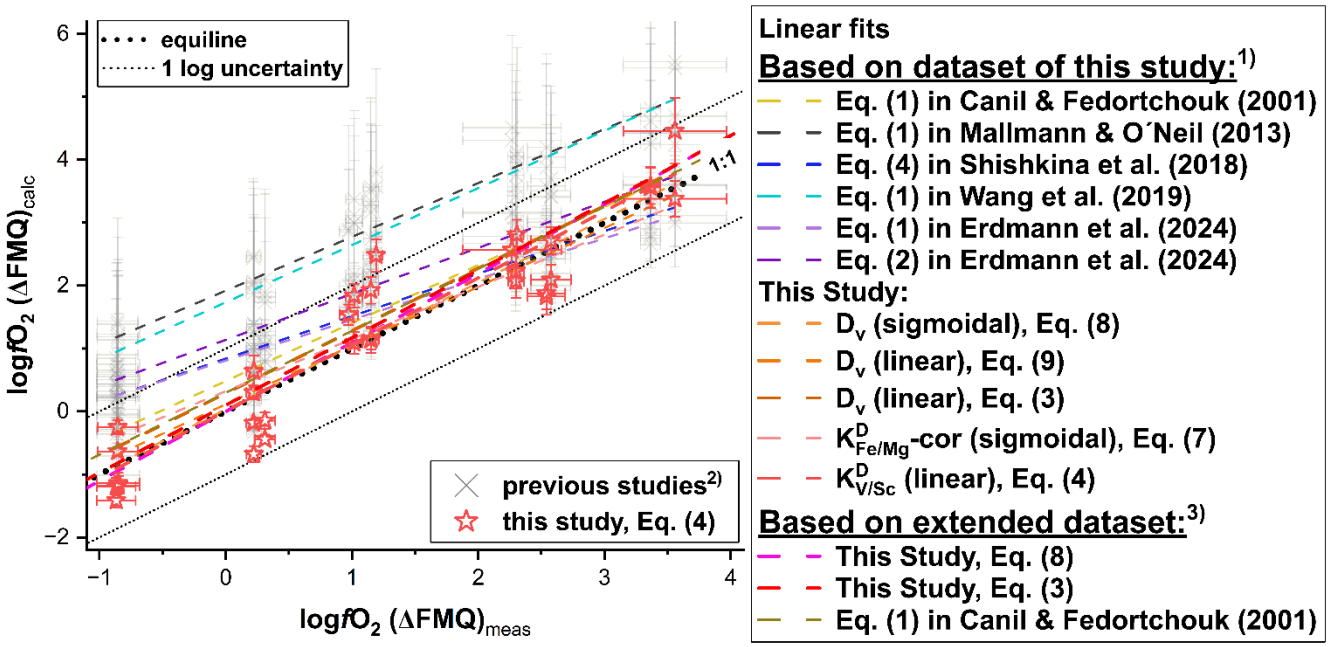

1476

1477 Figure 12

This manuscript is a **non-peer-reviewed preprint**. A **substantially revised and peer-reviewed version** has been published in: *Geochimica et Cosmochimica Acta*
https://doi.org/10.1016/j.gca.2025.12.025

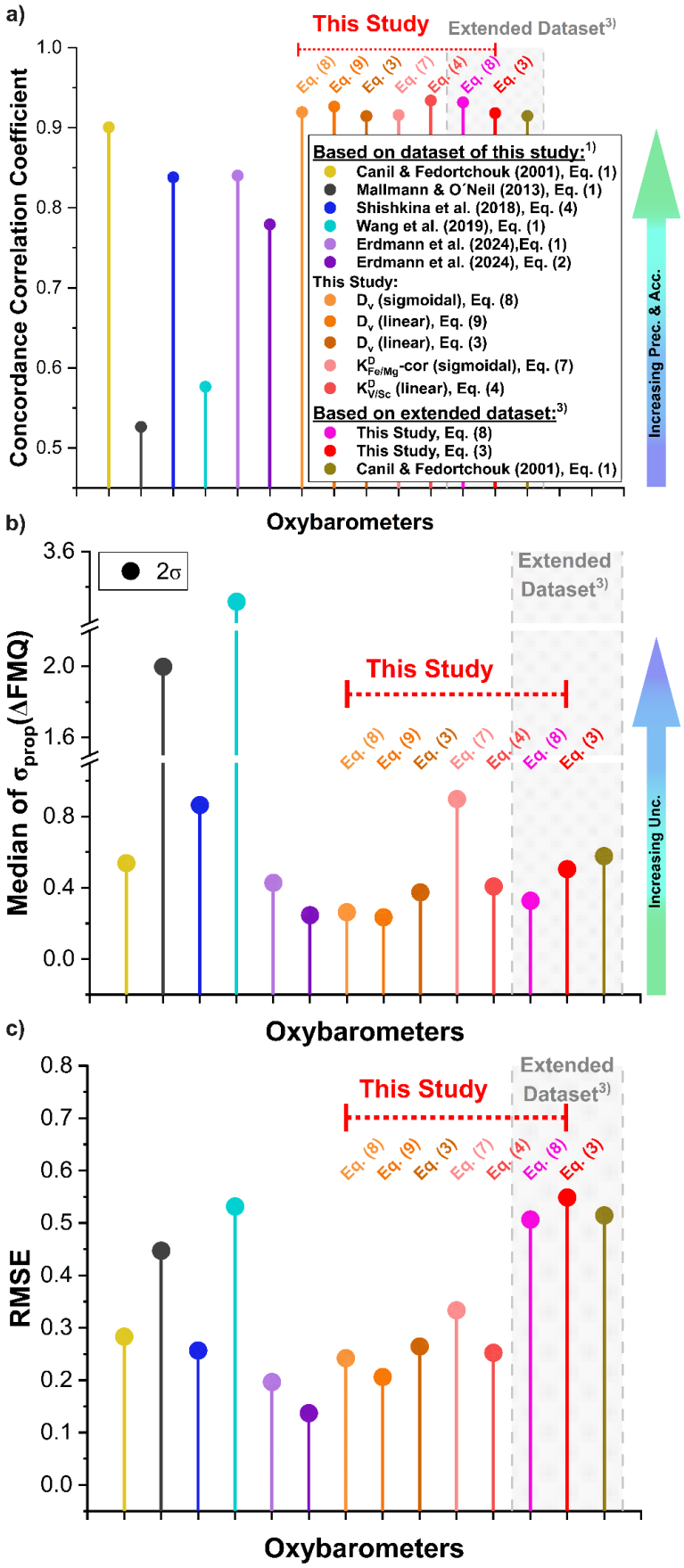

1478